



HAL
open science

3D phase-resolved wave modelling with a non-hydrostatic ocean circulation model

Patrick Marsaleix, Héloïse Michaud, Claude Estournel

► To cite this version:

Patrick Marsaleix, Héloïse Michaud, Claude Estournel. 3D phase-resolved wave modelling with a non-hydrostatic ocean circulation model. *Ocean Modelling*, 2019, 136, pp.28-50. 10.1016/j.ocemod.2019.02.002 . hal-03041724

HAL Id: hal-03041724

<https://hal.science/hal-03041724>

Submitted on 5 Dec 2020

HAL is a multi-disciplinary open access archive for the deposit and dissemination of scientific research documents, whether they are published or not. The documents may come from teaching and research institutions in France or abroad, or from public or private research centers.

L'archive ouverte pluridisciplinaire **HAL**, est destinée au dépôt et à la diffusion de documents scientifiques de niveau recherche, publiés ou non, émanant des établissements d'enseignement et de recherche français ou étrangers, des laboratoires publics ou privés.

See discussions, stats, and author profiles for this publication at: <https://www.researchgate.net/publication/341233096>

3D phase-resolved wave modelling with a non-hydrostatic ocean circulation model

Preprint · May 2020

CITATIONS

0

READS

106

3 authors, including:



Patrick Marsaleix

French National Centre for Scientific Research

127 PUBLICATIONS 3,335 CITATIONS

[SEE PROFILE](#)



Héloïse Michaud

Service hydrographique et océanographique de la marine

35 PUBLICATIONS 211 CITATIONS

[SEE PROFILE](#)

Some of the authors of this publication are also working on these related projects:



MERMEX-DEWEX [View project](#)



Development of unstructured WWIII [View project](#)

1 **3D phase-resolved wave modelling with a non-hydrostatic ocean circulation model**

2 Patrick Marsaleix (1), Héloïse Michaud (2), Claude Estournel (1)

3

4 (1) Laboratoire d'Aérodologie, Université de Toulouse, CNRS, UPS, 14 avenue Edouard Belin,
5 31400 Toulouse, France

6 (2) Shom – Antenne de Toulouse, 42 avenue G. Coriolis, 31057 Toulouse, France.

7

8 **Key words:** phase-resolved wave modelling, wave breaking, rip currents, non-hydrostatic,
9 ocean circulation model.

10

11 **Corresponding author:** Patrick Marsaleix, patrick.marsaleix@aero.obs-mip.fr

12

13 **Abstract**

14 A phase-resolved wave model is derived from an ocean circulation model for the purpose of
15 studying wave-current effects in nearshore zones. One challenge is to adapt the circulation
16 model to the specificities of wave physics. This mainly concerns the consideration of non-
17 hydrostatic effects and the parametrization of wave breaking. The non-hydrostatic pressure
18 is calculated using the *artificial compressibility method* (ACM). The ACM-induced errors on
19 wave dispersion properties are examined in detail in the context of the linear theory using
20 idealized test cases. The possible compromise between the precision achieved on non-
21 hydrostatic physics and the adjustable CPU cost of the ACM method is looked at in detail.
22 The modification of the wave characteristics by the bathymetric slope and the breaking of
23 waves are then examined from a linear slope beach laboratory experiment. Finally the model
24 is evaluated on the issue of rip currents and their feedback on the wave field using a
25 laboratory experiment of a beach with a bar intersected by channels.

26

27 **1 Introduction**

28

29 The interactions between waves and current play a major role in coastal modelling studies
30 and are important to correctly reproduce the nearshore circulation. Coastal engineering
31 applications need realistic descriptions of waves and currents, their transformations towards
32 the nearshore and behaviours with artificial coastal structures for the design of harbours or
33 dykes to prevent overtopping and to reduce submersion or erosion risks and this is only
34 possible with a circulation model that reproduces explicitly the waves. Taking into account
35 the waves in the circulation models allows on the one hand the representation of the residual
36 flows generated by the waves such as the Stokes drift (Mellor 2003) or the rip currents
37 (Castelle et al, 2016) and on the other hand, to take into account turbulence generation by
38 waves in the turbulent closure scheme, which improves the oceanic surface and bottom
39 boundary layers, the vertical current shear, and the vertical temperature and salinity profiles
40 in the circulation model (Uchiyama et al, 2010). In shallow waters, when the waves effects
41 near the bottom are no longer negligible, the bottom stress is significantly increased,
42 allowing the resuspension of sand and sediments (Soulsby, 1995), the Stokes drift, the
43 undertow or rip currents then playing an important role in their transport in the water column.
44 The wave-current interaction is also decisive for the mean surface level set-up during
45 storms, the modification of the surface stress related to the roughness created by the waves,
46 the modelling of the marine submersion of the coastal continental surfaces (Bertin et al,
47 2012), the modification of the coastline, the evolution of the shape of the seabed
48 (Bouharguane et al, 2010) .

49 At the spatial scales of the coastal circulation models (see review by Klingbeil et al,
50 2018), such studies are mainly done using a hydrostatic circulation model coupled with a
51 spectral phase-averaged wave model (McWilliams et al 2004, Ardhuin et al 2008, Bennis et
52 al, 2011, [Benetazzo et al, 2013](#), Kumar et al, 2015, Uchiyama et al, 2017). The phase-
53 averaged wave model feeds the circulation model with Stokes drift, residual wave pressure,
54 momentum and turbulence production terms related to wave erosion. In return, the
55 circulation model gives the wave model the variations of sea surface level and surface
56 current, the latter being able to significantly modify the wave field (Uchiyama et al., 2009) as

57 in the known example of rips current. The choice of a phase-averaged wave model is largely
58 guided by computational time considerations as it provides mean properties of the sea state.
59 The spectral model can indeed be used with a horizontal resolution much lower than the
60 wave wavelengths and therefore cover large areas with a reasonable number of grid points.

61 An alternative is the phase-resolved model, or deterministic model, that explicitly
62 describes the evolution of the free surface. The SWASH models (Zijlema et al, 2011),
63 REF/DIF (Kirby and Dalrymple, 1983), FUNWAVE (Kirby et al, 1998), BOSZ (Roeber and
64 Cheung, 2012), NHWAVE (Ma et al, 2012) are widespread examples of this type of model,
65 very often mentioned in the wave modelling literature. The processes resulting from the
66 effects of bathymetry such as refraction, diffraction and reflections (Magne et al, 2005),
67 interaction with other waves or with the background circulation, infragravity waves (Bertin et
68 al, 2018), the asymmetrical wave transformation at the approach of the breaking phase, are,
69 in principle, better represented by this type of model (Rusu and Soares, 2013). The phase-
70 resolved model is also well suited for sand mobilization, which is directly dependent on
71 orbital velocity near the bottom (Bouharguane et al, 2010). The phase-resolved model has a
72 continuous approach of frequencies and directions, while the phase-averaged model solves
73 its equations on a discrete spectrum of frequencies and directions which results in a relative
74 inaccuracy related to frequency and direction resolution. For example, in Michaud et al 2012,
75 the Wavewatch III r model (Tolman et al., 2016) is used with 36 discrete values of the
76 direction leading to a truncation of the direction of the waves of the order of 10° . However,
77 the phase-resolved models require finer temporal and spatial discretisation, thus larger
78 computational resources. The resolution of the horizontal grid imposes a limit on the
79 permissible wavelengths, truncating the shortest periods of the wave spectrum.

80 Deterministic nearshore models should have accurate dispersion and non-linear
81 properties and thus should be governed by the Navier–Stokes equations (Raoult et al.,
82 2016), using either an Eulerian approach (e.g., OpenFOAM®, Zhou et al., 2017) or a
83 Lagrangian approach (e.g. the meshless model SPH model, Oger, 2006). These models are
84 appropriate for local studies, although eventually limited by spurious diffusion or prohibitive

85 computational time (Benoit et al., 2017). Simplifications can be made to overcome these
86 problems: for instance, REF/DIF based on the mild slope equation (Berkhoff, 1972) neglects
87 some nonlinear effects; SWASH can be used with depth-averaged equations with
88 appropriate assumptions to introduce the non-hydrostatic pressure (Zijlema et al. ,2011);
89 Boussinesq, Serre (1953) or Green-Naghdi (Green and Naghdi, 1976) models take partially
90 into account non linear or dispersive effects (e.g., Bonneton et al.,2011a, 2011b, Tissier et
91 al., 2012).

92 Within the limits of the above simplifications, phase-resolved models should
93 theoretically be capable of simulating the low-frequency 3D processes usually modelled by
94 circulation models, since their equations are basically the same, except for the hydrostatic
95 assumption generally made in circulation models (Klingbeil et al. , 2018). As a result, the
96 phase-resolved wave model is able to generate residual currents such as rip currents and
97 therefore does not require coupling with a circulation model to simulate the coupling between
98 waves and low frequency fields. However, it requires a significant horizontal and vertical
99 resolution (greater than the wavelength of the waves) which limits the size of the modelled
100 domain. To date and to our knowledge, most of the applications of the phase-resolved
101 models seem to concern domains whose horizontal dimensions are of the order of a few
102 kilometres in each horizontal direction (Yoon, 2014). The constant rise of computers
103 capability suggests that phase-resolved models could now be used on larger domains
104 covering a significant part of the continental shelf. Meanwhile, ocean circulation models
105 currently used at coastal scales could be adapted to deterministic wave modelling with,
106 (among other objectives), the goal of linking waves and continental shelf circulations like
107 wind-induced eddies (Petrenko et al. 2008), or to better understand momentum and
108 turbulence transfer in the surface layer (Deigaard and Nielsen, 2018). This assumes,
109 however, that their equations are suitable for phase-resolved wave modelling. One of the
110 essential points is to be able to use these models in non-hydrostatic mode. A number of
111 articles deal with this question, for the MITgcm model (Marshall et al., 1997), POM
112 (Kanarska and Maderich, 2003), ROMS (Kanarska et al, 2007), GETM (Klingbeil and

113 Burchard, 2013), SYMPHONIE (Auclair et al, 2011). However, at the resolutions where
114 these models are most often used, the consideration of non-hydrostatic effects may not be
115 an essential issue (McKiver et al, 2016). The applications envisaged so far concern more the
116 propagation of internal gravity waves (Bordois et al 2017) or the convective processes
117 (Paluszkiwicz et al, 1994) than the high frequency surface waves. One of the obstacles to
118 the deterministic modelling of waves over large domains is the cost of the non-hydrostatic
119 solver (Klingbeil et al, 2018). As previously mentioned, in the field of phase-resolved wave
120 modelling, the common alternative to this difficulty is to use simplified models adapted to the
121 physical specificities of waves (Bonneton et al.,2011a, 2011b). In the field of ocean
122 circulation modelling, the most widespread approach to the non-hydrostatic problem, on the
123 contrary, is to take into account the whole complexity of the problem. It leads concretely to
124 the resolution of a Poisson equation for the non-hydrostatic pressure. This is a global
125 approach insofar as this leads to a system of linear equations making all the points of the
126 numerical domain interdependent. Its resolution is in principle costly and currently
127 constitutes a challenge in the perspective of large numerical domains of several thousand
128 points in each direction (Roulet et al., 2017). The sigma coordinate widely used in coastal
129 modelling also increases the cost of the resolution for two main reasons. The first reason is
130 that the time variation of the position of the vertical levels (related to the movement of the
131 free surface) forces to update regularly the coefficients of the main matrix of the system and
132 its possible preconditioning. The possible representation of the wetting-drying zones adds a
133 similar difficulty. The second reason is that the sigma coordinate transformation increases
134 the number of nonzero coefficients of the principal matrix. Roulet et al. 2017 propose to
135 reduce this number by reformulating the momentum equations. The same authors also
136 evoke the perspective of the multigrid approach to significantly reduce the cost of
137 calculation. An application in the vertical direction is proposed by Shi et al. (2015).

138 The alternative to the global approach is the local approach based on the direct
139 resolution of non-hydrostatic pressure. Various methods have been proposed so far (Johns
140 1991, Klingbeil and Burchard, 2013, Bordois et al, 2017, Lee et al, 2006). Among them, Lee

141 et al, 2006 (hereafter L06) ACM (artificial compressibility method) method has a reasonable
142 numerical cost and its implementation in a model is easy. A method derived from L06 is
143 implemented in the SYMPHONIE circulation model (Marsaleix et al, 2008) and tested in the
144 aforementioned context, namely the high frequency surface waves and the associated
145 residual circulations. The purpose of the present paper is to assess this model on the
146 principal issues of wave modelling. This concerns on the one hand the dispersion properties,
147 the vertical shear of the current, the asymmetrical wave transformation at the approach of
148 the breaking conditions, the decay of the waves in the breaking zone. On the other hand,
149 this concerns the residual waves-related circulation such as the stokes transport, the
150 alongshore coastal drift, the mean sea level, rip currents and their feedback on the waves.
151 The article is organized as follows: chapter 2 deals with the implementation of the ACM
152 method in the ocean circulation model, [chapter 3 gives an analytical solution verifying the](#)
153 [ACM equations for low amplitude waves](#), chapter 4 describes academic and laboratory test
154 cases and finally chapter 5 provides a summary and the conclusions.

155

156 **2 Model description**

157

158 *2.1 Equations*

159

160 For the sake of clarity the problem is first presented in a simplified way, in a vertical 2D plane
161 and presenting only the terms that dominate wave physics:

162

$$163 \quad \frac{\partial u}{\partial t} = -g \frac{\partial \eta}{\partial x} - \frac{\partial q}{\partial x} \quad (1)$$

164

$$165 \quad \frac{\partial w}{\partial t} = -\frac{\partial q}{\partial z} \quad (2)$$

166

167

168 where q is the non-hydrostatic pressure times the water density, u and w the horizontal and
 169 vertical current, η the sea surface height. As in L06 the hypothesis of incompressibility is
 170 retained to deduce the surface elevation:

171

$$172 \quad \frac{\partial \eta}{\partial t} = -\frac{\partial}{\partial x} \int_{-h}^{\eta} u dz \quad (3)$$

173

174 Equation (2) is in practice not calculated by the model. Instead, the combination of (1) and
 175 (2) that leads to the Poisson equation is used:

176

$$177 \quad \frac{\partial}{\partial t} \left(\frac{\partial u}{\partial x} + \frac{\partial v}{\partial y} + \frac{\partial w}{\partial z} \right) = -g \left(\frac{\partial^2 \eta}{\partial x^2} - \frac{\partial^2 q}{\partial x^2} - \frac{\partial^2 q}{\partial z^2} \right) \quad (4)$$

178

179 The left-hand side of the Poisson equation is ideally zero in the case of the incompressible
 180 hypothesis. Without questioning this hypothesis of incompressibility, the particularity of the
 181 L06 method is however to allow the left-hand side of (4) to be small and not to equal zero.
 182 Before detailing the approach of L06, some comments can be made on the possibility of not
 183 cancelling strictly the left-hand side of (4). It can be noted, for example, that non-hydrostatic
 184 incompressible models can use iterative solvers whose convergence is *de facto* imperfect,
 185 precluding a strict cancellation of the left-hand side of (4). This approximation is currently
 186 accepted because the physical coherence is preserved if the convergence of the solver is
 187 sufficiently precise. We can also recall that a model such as the one used in this study does
 188 not formally represent (4) but its discrete approximation in the finite difference sense. Not
 189 strictly cancelling the left-hand side of (4) induces an error whose order of magnitude can be
 190 compared to the discretization errors of the other terms. For example, given the numerical
 191 scheme used here, the error made on the horizontal laplacian of q at the right-hand side of
 192 (4) is of the order of (APPENDIX A):

193

$$194 \quad \frac{dx^2}{12} \frac{\partial^4 q}{\partial x^4} \approx \frac{dx^2}{12} k^4 q \quad (5)$$

195

196 where k is the wavenumber. This discretization error makes it possible to consider a possible
197 error on the left-hand side, thus relativizing the question to the transformation of the left-hand
198 side of (4) into a term of artificial compressibility as described by L06 (see equation 2 in
199 L06). In practice, the ACM method of L06 leads to the reformulation of (4) as follows:

200

$$201 \quad \frac{1}{\alpha^2} \frac{\partial^2 q}{\partial t^2} = g \frac{\partial^2 \eta}{\partial x^2} + \frac{\partial^2 q}{\partial x^2} + \frac{\partial^2 q}{\partial z^2} \quad (6)$$

202

203 Assuming a sinusoidal form for q , the artificial compressibility term at the left-hand side of
204 (6) is of the same order as $\left(\frac{\omega}{\alpha}\right)^2 q = \left(\frac{c}{\alpha}\right)^2 k^2 q$ (c is the celerity of the waves), which, under
205 certain conditions, can become of an order of magnitude comparable to (5) (ie $\left(\frac{c}{\alpha}\right)^2$
206 comparable to $\frac{dx^2}{12} k^2$), insofar as it is recommended to use the ACM method with α such that
207 $\left(\frac{c}{\alpha}\right)^2 \ll 1$. This point is closely examined later in the article.

208

209 In fact, ideally, in compressible theory, the α constant should be the speed of the
210 acoustic waves, actually much higher than c . However, as pointed out by Mahadevan et al
211 (1996), this would have the consequence of requiring an extremely small time step, highly
212 increasing the computational cost. This type of approach therefore generally uses a much
213 lower α value in order to increase the time step and thus makes the cost of the calculation
214 affordable. It is therefore noted that the true compressibility of the ocean is not respected by
215 this approach which relies more on numerical considerations than on a real physical
216 justification (resulting in the expression "*artificial compressibility*" used by L06). On the other
217 hand, apart from the equation (6), the other equations of the model strictly respect the
218 incompressibility framework. Although greatly diminished by the computational time
219 constraint just mentioned, the value of α must nevertheless remain sufficiently large to allow
219 rapid adjustment of equation (6) to variations in the hydrostatic forcing terms. This property

220 is essential for the accuracy of the non-hydrostatic behavior of the model. In practice, α must
 221 remain larger than the phase speed of gravity waves (Bordois et al, 2017).

222 The resolution of the Poisson iterative equation (6) can be done with the same time step as
 223 the other equations. In practice its determination is done from the stability criterion
 224 corresponding to the forward-backward scheme, but considering α rather than the speed of
 225 the gravity waves as it is larger. The time step is therefore smaller than the one of a
 226 hydrostatic model in similar conditions, but the calculation nevertheless remains affordable
 227 (as we will see in the following) because equation (6) is computed only once per time step of
 228 the full model.

229

230 *2.2 Implementation in the SYMPHONIE model*

231

232 The model used is the ocean circulation model SYMPHONIE (Marsaleix et al. 2008).
 233 As we focus on surface waves, the effect of temperature and salinity is neglected. For the
 234 sake of clarity the equations are given in a Cartesian coordinate system but the model
 235 actually uses a system of generalized sigma coordinates. The momentum equations are
 236 given by:

237

$$238 \quad \frac{\partial u}{\partial t} = -\frac{\partial uu}{\partial x} - \frac{\partial vu}{\partial y} - \frac{\partial wu}{\partial z} + fv - g\frac{\partial \eta}{\partial x} - r\frac{\partial q}{\partial x} + \frac{\partial}{\partial z}\left(K_m \frac{\partial u}{\partial z}\right) + \tau_u \quad (7)$$

$$239 \quad \frac{\partial v}{\partial t} = -\frac{\partial uv}{\partial x} - \frac{\partial vv}{\partial y} - \frac{\partial wv}{\partial z} - fu - g\frac{\partial \eta}{\partial y} - r\frac{\partial q}{\partial y} + \frac{\partial}{\partial z}\left(K_m \frac{\partial v}{\partial z}\right) + \tau_v \quad (8)$$

$$240 \quad \frac{1}{\alpha^2} \frac{\partial^2 q}{\partial t^2} = -\frac{\partial}{\partial x}\left(\frac{\partial u}{\partial t}\right)^* - \frac{\partial}{\partial y}\left(\frac{\partial v}{\partial t}\right)^* + \frac{\partial^2 q}{\partial x^2} + \frac{\partial^2 q}{\partial y^2} + \frac{\partial^2 q}{\partial z^2} \quad (9)$$

241

242 Where $\left(\frac{\partial u}{\partial t}\right)^*$ and $\left(\frac{\partial v}{\partial t}\right)^*$ represent hydrostatic terms (in practice all the terms of the right-
 243 hand side of (7) and (8) except $r\frac{\partial q}{\partial x}$ and $r\frac{\partial q}{\partial y}$). *At this stage, r at the right-hand side of (7)*
 244 *and (8) is equal to one but we will see later that a value other than 1 can be used to improve*

245 [the accuracy of the dispersion relation and currents of short waves](#). The incompressibility
 246 hypothesis gives the vertical velocity and elevation of the surface:

247

$$248 \quad \frac{\partial u}{\partial x} + \frac{\partial v}{\partial y} + \frac{\partial w}{\partial z} = 0 \quad (10)$$

$$249 \quad \frac{\partial \eta}{\partial t} = -\frac{\partial}{\partial x} \int_{-h}^{\eta} u dz - \frac{\partial}{\partial y} \int_{-h}^{\eta} v dz \quad (11)$$

250

251 The vertical diffusion coefficient is calculated by the k-epsilon scheme (Rodi, 1987) and
 252 (τ_u, τ_v) are breaking terms parameterized as a horizontal diffusion:

253

$$254 \quad \tau_u = \frac{\partial}{\partial x} \left(\nu_b \frac{\partial u}{\partial x} \right) + \frac{1}{2} \frac{\partial}{\partial y} \left(\nu_b \left(\frac{\partial u}{\partial y} + \frac{\partial v}{\partial x} \right) \right) \quad (12)$$

$$255 \quad \tau_v = \frac{\partial}{\partial y} \left(\nu_b \frac{\partial v}{\partial y} \right) + \frac{1}{2} \frac{\partial}{\partial x} \left(\nu_b \left(\frac{\partial u}{\partial y} + \frac{\partial v}{\partial x} \right) \right) \quad (13)$$

256

257 The eddy viscosity of breaking ν_b is calculated from a breaking criterion which will be
 258 discussed in a section to follow. Bottom and surface boundary conditions are as follows: at
 259 the surface $q=0$, $\frac{\partial(u,v)}{\partial z} = 0$ and at the bottom $\frac{\partial q}{\partial z} = 0$, $\rho_0 K_m \frac{\partial(u,v)}{\partial z} = (\tau_b^x, \tau_b^y)$ where ρ_0 is the
 260 sea water density and (τ_b^x, τ_b^y) are the components of the bottom stress. The bottom stress
 261 is parameterized as in Blumberg and Mellor (1987), from a quadratic relationship of the
 262 bottom current and a drag coefficient derived from a roughness length.

263 The equations are calculated with a forward-backward time scheme detailed in
 264 APPENDIX B. Considering that short surface waves are intrinsically three-dimensional, the
 265 barotropic-baroclinic time splitting commonly used in circulation models for calculating
 266 separately barotropic and baroclinic velocities (Blumberg and Mellor 1987) can not applied
 267 here. In practice, all the equations are calculated with the same time step.

268

269 *2.3 The time step*

270

271 The time step is determined from the stability criterion specific to the forward-
272 backward scheme. In the case of the hydrostatic model, the criterion of stability with respect
273 to surface waves would be:

274

$$275 \quad dt_{max} = \frac{dx}{\sqrt{2}} \frac{1}{\sqrt{gh_{max}}} \quad (14)$$

276

277 where dx is the horizontal resolution, h_{max} is the maximum depth of the domain and
278 therefore $\sqrt{gh_{max}}$ is the maximum theoretical phase speed expected for surface waves. In
279 the non-hydrostatic model, the calculation of the equation for q imposes a more drastic
280 additional criterion since it depends on α that is greater than $\sqrt{gh_{max}}$. It is not trivial to find a
281 simple expression similar to (14) but, unsurprisingly, it appears in simulations performed by
282 the authors that the maximum value of the time step allowed by the non-hydrostatic model
283 was close to $\frac{dx}{\sqrt{2}} \frac{1}{\alpha}$, ie (14) with $\sqrt{gh_{max}}$ replaced by α . In practice, in all the simulations
284 presented, the time step of the non hydrostatic model is given by a fraction (70%) of this
285 criterion to include other stability criteria than gravity waves such as those resulting from
286 non-linearities, namely:

287

$$288 \quad dt = 0.7 \frac{dx}{\sqrt{2}} \frac{1}{\alpha} \quad (15)$$

289

290 The determination of α is therefore related to the determination of the time step. The larger
291 the first, the smaller is the second. The quantity N which represents the ratio of the
292 theoretical time step of the hydrostatic case to the time step of the non-hydrostatic case, is
293 introduced:

294

$$295 \quad N = \frac{dt_{max}}{dt} \quad (16)$$

296

297 which, using (14) and (15), is equivalent to

298

$$299 \quad N = \frac{1}{0.7} \frac{\alpha}{\sqrt{gh_{max}}} \quad (17)$$

300

301 N is a key parameter of the problem. The larger it is, the smaller is the model time step and
302 the better is the accuracy expected on the non-hydrostatic term. Since dt_{max} , is the time
303 step that would normally have the hydrostatic model in similar conditions, the ratio N is a
304 good indicator of the relative additional cost associated with the non hydrostatic effect. The
305 evaluation of this additional cost must also take into account that an additional equation (for
306 q) has been added to the equations of the hydrostatic model. The latter essentially counts 4
307 three-dimensional equations, two for the horizontal components of the current, one for the
308 turbulent kinetic energy and one for its dissipation rate. The relative numerical excess cost of
309 the equation for q is therefore of the order of $N \frac{4+1}{4} = 1.25 N$.

310

311 **3 Analytical solutions**

312

313 Analytical solutions verifying model equations in the context of linear theory are now
314 presented. We consider a 2D vertical plan, a linearized version of (7),

315

$$316 \quad \frac{\partial u}{\partial t} = -g \frac{\partial \eta}{\partial x} - r \frac{\partial q}{\partial x} \quad (18)$$

317

318 the continuity equation,

319

$$320 \quad \frac{\partial u}{\partial x} + \frac{\partial w}{\partial z} = 0 \quad (19)$$

321

322 and the non-hydrostatic pressure equation (6). The elevation of the surface is of the form

323 $\eta = \eta_0 e^{i(kx - \omega t)}$. The non-hydrostatic pressure satisfying equation (6) is of the form:

324

325
$$q = -(g/\mu^2)\eta + 2P^0 e^{i(kx - \omega t)} \cosh(\mu k(z + h)) \quad (20)$$

326

327 with

328

329
$$\mu^2 = \left(1 - \frac{\omega^2}{k^2 \alpha^2}\right) \quad (21)$$

330

331 Where α appears in the left hand side of (6) and in the definition of N calculated by (17).

332 Using (20) and the surface condition $q=0$ leads to:

333

334
$$q = \frac{g}{\mu^2} \eta (-1 + \cosh(\mu k(z + h)) / \cosh(\mu kh)) \quad (22)$$

335

336 Using (22) and (18) gives the horizontal current:

337

338
$$u = g \frac{k}{\omega} \eta \left[1 + \frac{r}{\mu^2} \left(\frac{\cosh(\mu k(z+h))}{\cosh(\mu kh)} - 1\right)\right] \quad (23)$$

339

340 Using (23) and the continuity equation (19) to derive the vertical velocity, then applying the

341 surface condition $w = \frac{\partial \eta}{\partial t}$, leads to the dispersion relation:

342

343
$$\omega^2 = k^2 g \left(1 - \frac{r}{\mu^2}\right) h + \frac{r}{\mu^3} g k \tanh(\mu kh) \quad (24)$$

344

345 Note that if $r=1$ and if N (therefore α) tends to infinity (leading to the cancellation of the left-

346 hand side of (6) and $\mu = 1$) the dispersion relation (24) becomes equivalent to the usual

347 dispersion relation (Kinsman, 1965):

348

349 $\omega^2 = gk \tanh(kh)$ (25)

350

351 while, using (23) and (25), we find the usual solution for the horizontal current (Kinsman,
352 1965):

353

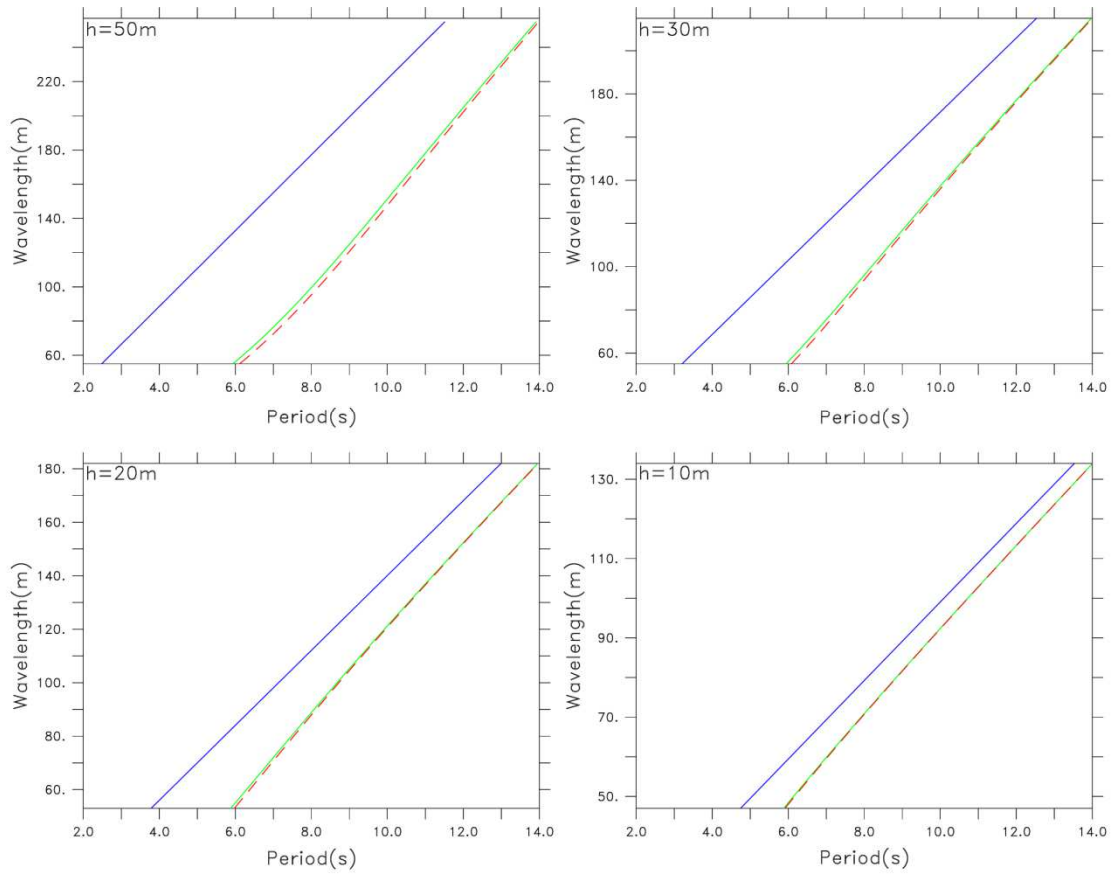
354 $u = \omega\eta \frac{\cosh(k(z+h))}{\sinh(kh)}$ (26)

355

356 This result shows that the ACM method becomes equivalent to the classical non-
357 hydrostatic incompressible method if N is sufficiently large. In the following, we distinguish
358 the dispersion relations of the incompressible non-hydrostatic linear theory (ie (25)), of the
359 non-hydrostatic ACM theory (ie (24)) and of the hydrostatic theory (ie (27)):

360

361 $\omega/k = \sqrt{gh}$ (27)



362

363 *Figure 1. Dispersion relations at different bottom depth. Blue line: hydrostatic linear theory (27).*

364 *Green line: incompressible non-hydrostatic theory (25). Dashed red line: ACM theory (24) with $r=1$*

365 *and $N = 5$.*

366

367 *Figure 1 shows these different dispersion relations for periods ranging from 6s to 14s*

368 *(this choice will be discussed in the next section), for different bathymetry values and $N=5$.*

369 *The ACM theory with $r=1$ provides a considerable improvement over the hydrostatic theory*

370 *but overestimates the non-hydrostatic effect (Figure 1: the dashed red curve is always below*

371 *the green curve). This overestimation increases with bathymetry. At shallow depths the*

372 *agreement is very satisfactory, but the non-hydrostatic effect is also less significant (Figure*

373 *1, $h=10m$).*

374

375 The parameter r is a way to bring ACM theoretical solution closer to the non-
 376 hydrostatic incompressible theory. Frequencies produced by (24) and (25) are actually
 377 equivalent if

378

$$379 \quad r = \mu^3 \frac{\tanh(kh) - kh}{\tanh(\mu kh) - \mu kh} \quad (28)$$

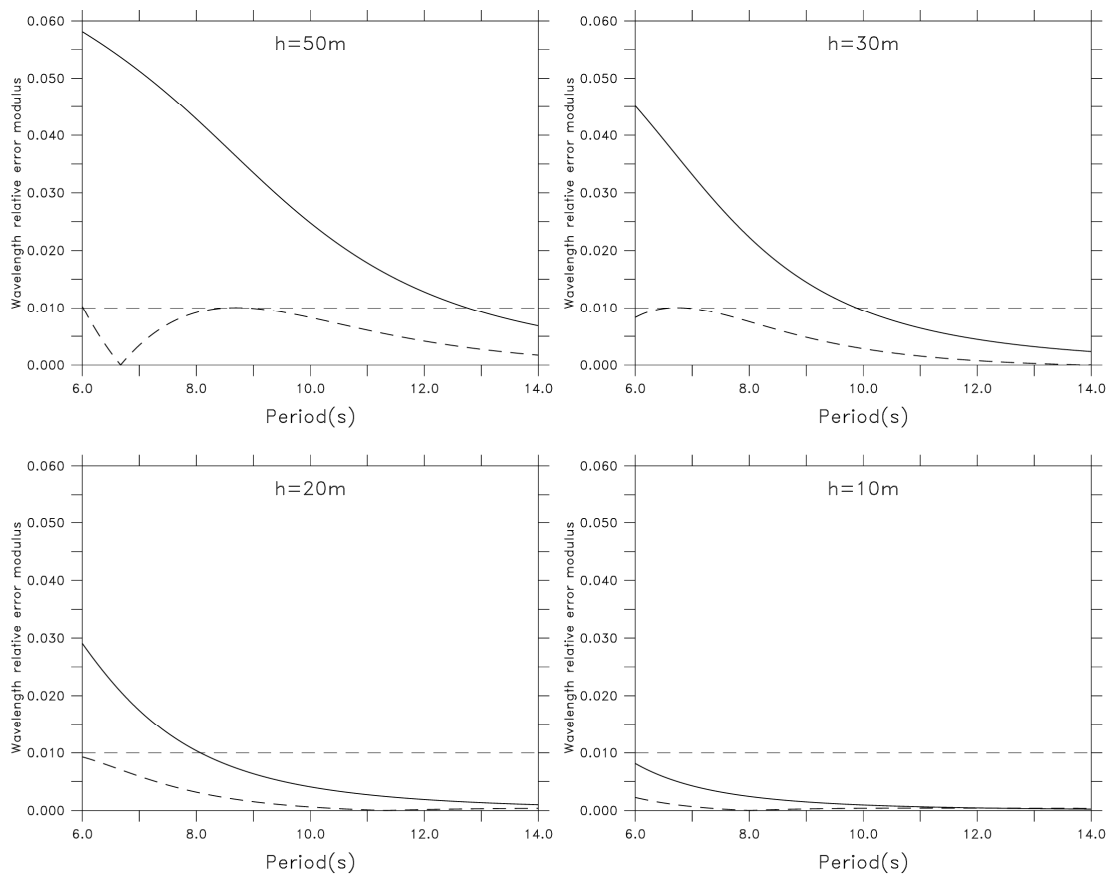
380

381 Horizontal currents (23) and (26) are identical on the surface without condition on r and μ ,
 382 while near the bottom they are equivalent if

383

$$384 \quad r = \mu^2 \left(\frac{1}{\cosh(kh)} - 1 \right) \left(\frac{1}{\cosh(\mu kh)} - 1 \right)^{-1} \quad (29)$$

385



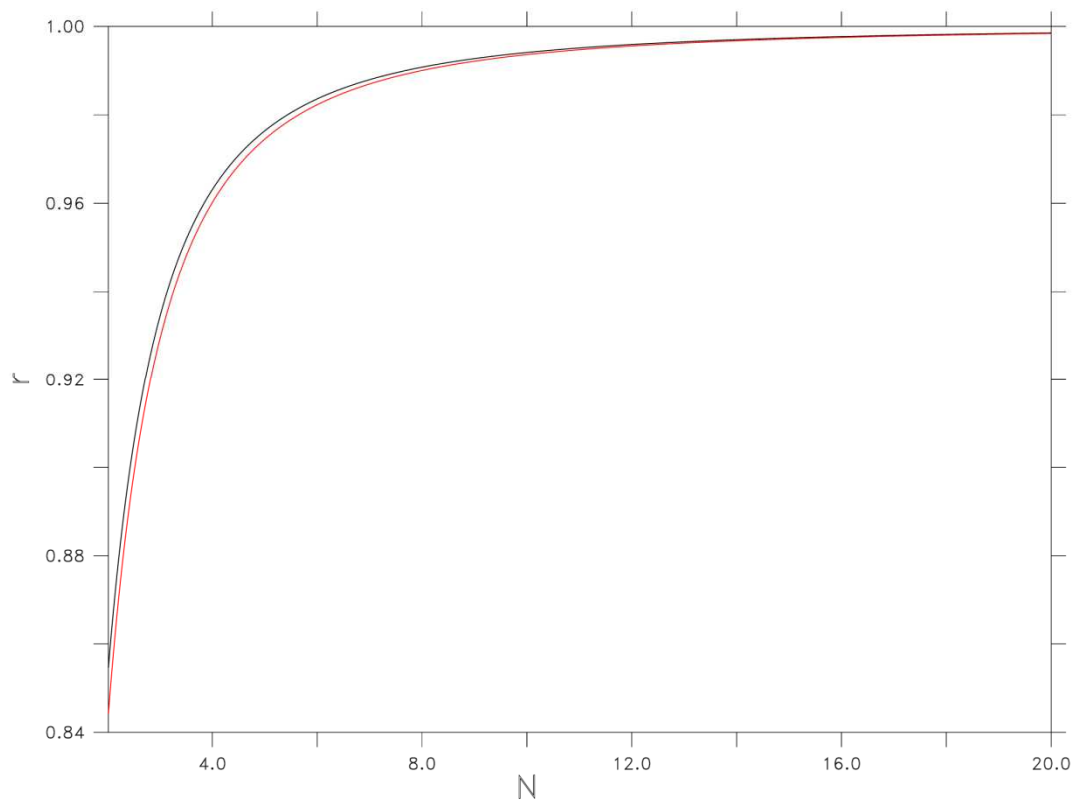
386

387 *Figure 2. Relative error on the wavelength computed by the ACM dispersion relation (24) at different*
388 *bottom depth and $N=5$. Solid line: $r=1$. Dashed line $r=0.9845$. The horizontal dashed line indicates*
389 *an error level of 1%.*

390

391 Expressions (28) and (29) suggest the possibility of optimizing r according to the
392 local values of the depth and the dominant period of waves. This point will be addressed in
393 future applications. At this early stage of our study, r will be considered constant. *Figure 2*
394 *shows the absolute value of the relative error on the wavelength, $|L_{ACM} - L|/L$, as a function*
395 *of the period, L_{ACM} being deduced from (24) and L , the “true” wavelength, from (25).*
396 *Relative errors are more important for small periods and for large bathymetry values. Errors*
397 *of the order of several % are expectable with $r = 1$. On the other hand, it is possible to*
398 *reduce the error level below 1%, for all the values of period and bathymetry considered in*
399 *Figure 2, with $r = 0.9845$.*

400 The fact that (28) and (29) are not identical shows that it is not possible to strictly
401 cancel the error on the current and on the dispersion relation with the same value of r .
402 However as shown in *Figure 3* for $h=50m$ and a period of 10s, (28) and (29) give very similar
403 values of r so that it is possible to find a value of r that reduces both the current and
404 dispersion relation errors (this will be discussed in the next section). Finally we note that a
405 compromise on these two possible values of r is all the easier to find if N is large because
406 (28) and (29) converge both to $r=1$.



407
 408 *Figure 3: r computed with (28) (Black line) and (29) (red line) as a function of N for $h=50\text{m}$ and a*
 409 *period of 10s.*

410

411 In conclusion, the analytical solutions corresponding to the linearized equations of the ACM
 412 method show a satisfactory representation of the non-hydrostatic effect in the range of
 413 periods concerned by the future applications of the model to the near shore zone. The
 414 accuracy however depends on the setting of parameters such as N and r . Since the
 415 accuracy of a numerical model also depends on many other factors related to the
 416 discretization of equations, such as spatio-temporal resolution and relevance of numerical
 417 schemes, the above theoretical analysis is now completed with numerical experiments.

418

419 **4 Test cases**

420

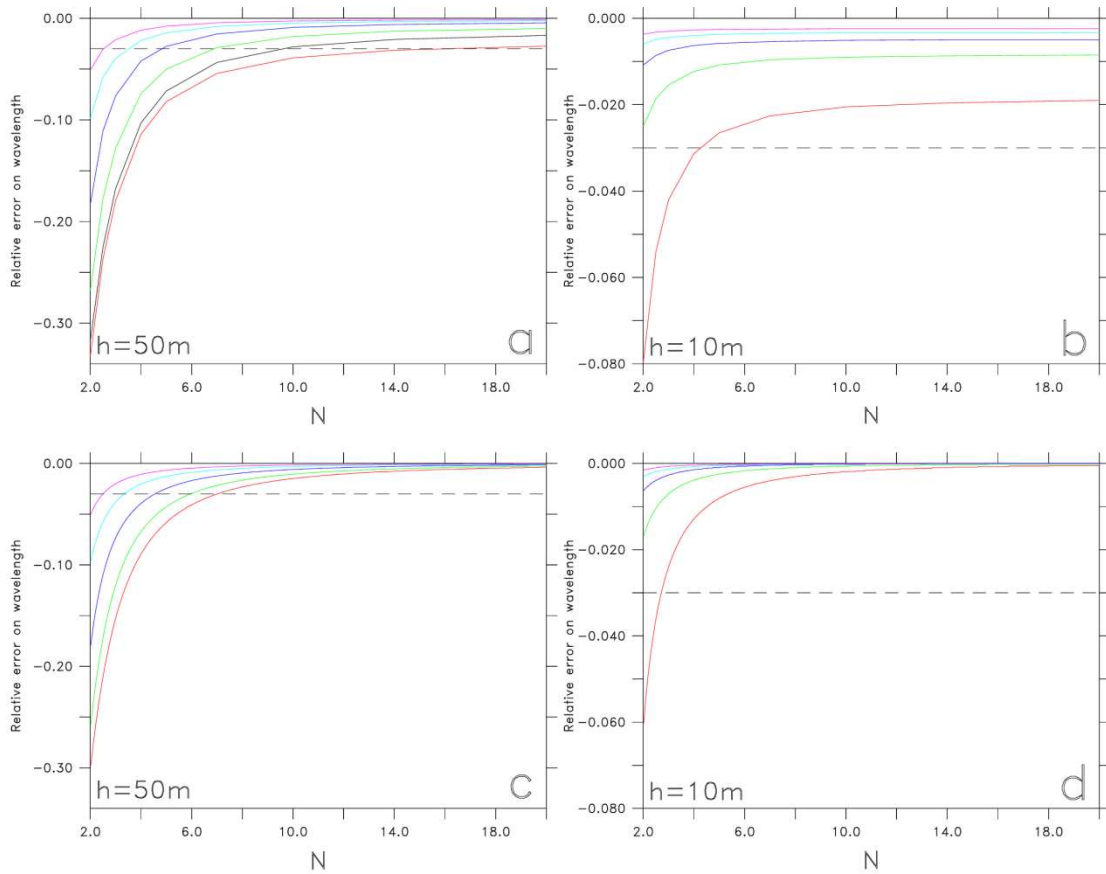
421 [4.1 Wave propagation in the context of linear theory](#)

422

423 In this section, we check the ability of the model to correctly represent the physical
424 characteristics of the simulated wave thanks to a series of test cases consisting in exploring
425 the dispersion properties of the waves. We consider here low amplitude waves (1 mm) in
426 order to be within the framework of the linear approximation for which simple analytical
427 solutions exist ([Kinsman, 1965](#)). The objective is to define the values of N which lead to a
428 reasonable compromise between the computation cost (consideration encouraging to lower
429 N) and the precision of the dispersion properties (consideration encouraging to increase N).
430 We use a domain with a flat bottom at 50 m depth, a periodic condition in the direction
431 normal to wave propagation. The horizontal resolution is 5m and 20 vertical levels are used.
432 The waves are generated at the entrance of the domain, while the fields are at rest at the
433 initial state. The opposite boundary is closed but the dimension in the direction of
434 propagation is large enough, so that the waves do not have time to reflect on it before the
435 end of the simulation (10 minutes). [This first numerical experiment is carried out with \$r = 1\$.](#)

436 [The open boundary conditions are derived from Marsaleix et al \(2006\). As](#)
437 [recommended by Blayo and Debreu \(2005\), an outgoing field is defined as the difference](#)
438 [between the total field and the incoming field. We thus define anomalies of currents, sea](#)
439 [surface height and non-hydrostatic pressure, \$u' = u - u_w\$, \$\eta' = \eta - \eta_w\$, \$q' = q - q_w\$ where](#)
440 [\$u_w, \eta_w, q_w\$ are prescribed by the analytical solution of the short wave linear theory. We then](#)
441 [assume that the incoming short waves do not reflect at the coast because of dissipation and](#)
442 [that waves propagating offshore are at lower frequencies \(they may consist of infra-gravity](#)
443 [waves if the conditions of their generations are met \(Bertin et al, 2018\)\). The radiative](#)
444 [conditions, \$u' = \pm g\eta'/c\$ and \$\partial q'/\partial t \pm c\partial q'/\partial x = 0\$, are therefore applied using the long](#)
445 [wave phase speed \$c = \sqrt{gh}\$.](#)

446 The simulation is analyzed in order to extract the modelled wavelength and to
447 compare it with that predicted by the [theoretical relation dispersion of the incompressible](#)
448 [linear theory \(25\)](#). The modelled wavelength is diagnosed from the distance separating two
449 successive identical values of the surface level in the direction of propagation. The grid
450 points chosen for the calculation of this diagnosis are located beyond a distance of 625m
451 from the open boundary and, moreover, the diagnosis is only calculated once the transient
452 regime is reached (i.e. once the wave front has passed these points). A time average of the
453 values obtained is finally calculated. A set of simulations is done to estimate the precision on
454 [\(25\)](#) as a function of N (ranging from 2 to 20) and of the wave period. The smallest period
455 considered here is 6 seconds, associated with a wavelength of 56m for $h=50m$, represented
456 by 11 grid points given the horizontal resolution of 5m. This minimum value is considered as
457 a reasonable threshold with respect to the capacity of the C-grid to represent the small
458 wavelengths. The maximum period considered is 14 s which is associated with a wavelength
459 of approximately 250 m. Periods greater than 14s are not considered because their
460 wavelengths, much larger than the depths envisaged, render them slightly non-hydrostatic
461 and therefore not interesting from the point of view of the authors.



462

463 *Figure 4: Relative error on the wavelength $(L^* - L)/L$ where L is given by the incompressible linear*
 464 *theory and L^* is either deduced from simulations with 20 vertical levels and $dx=5m$ (figures a and b)*
 465 *or from the ACM linear theory (figures c and d). The horizontal dashed line indicates a relative error*
 466 *of -3%. Each curve corresponds to a period: 14s (magenta), 12s (cyan), 10s (blue), 8s (green), 6s*
 467 *(red). The black curve (figure a) corresponds to a period of 6s and $dx=2.5m$. $h=50m$ (figures a and*
 468 *c), or $h=10m$ (figures b and d)*

469

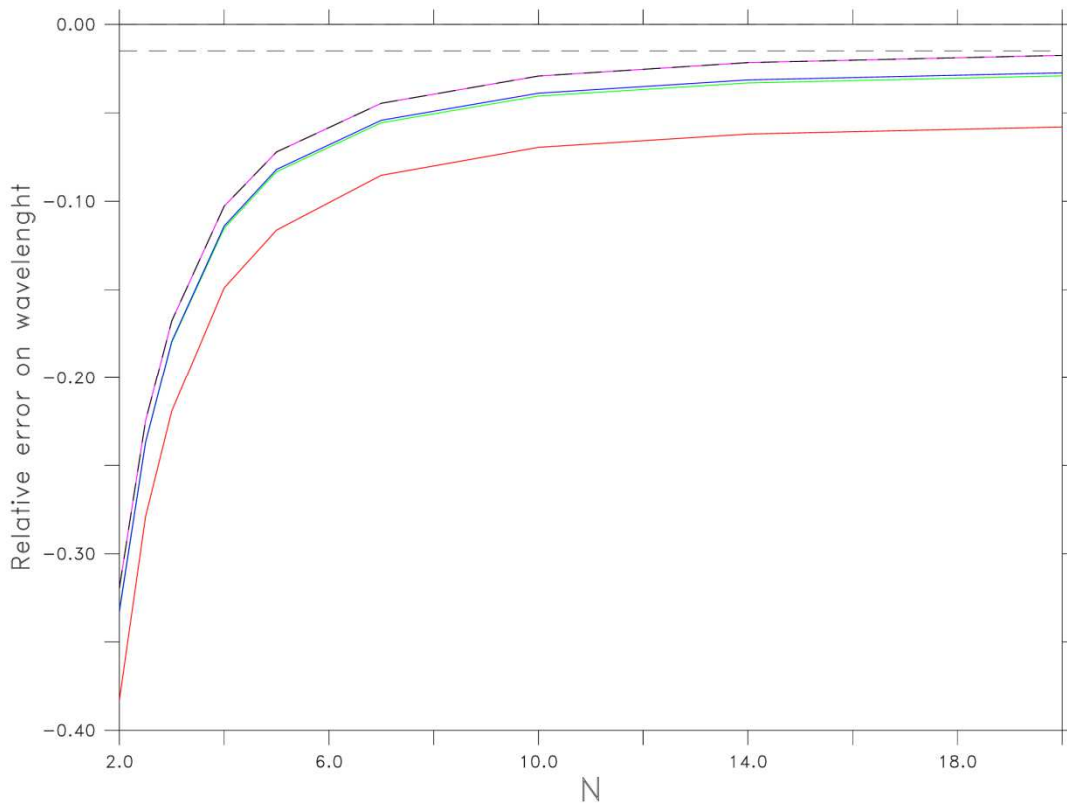
470

471 *Figure 4 shows the relative error on the wavelength, $(L^* - L)/L$, where the “true” wavelength*
 472 *L is given by the incompressible linear theory (25) and L^* is either deduced from the model*
 473 *or from the ACM linear theory (24) with $r=1$. Errors decrease when N increases. As expected*
 474 *from the previous section, the errors are stronger when the bottom depth is important. This*

475 could be an issue near the model open boundaries where the most important depths are
476 normally expected. To our knowledge, near shore modelling studies mostly focus on areas
477 where bathymetry does not exceed a few tens of meters. We thus assume that 50m could
478 be a plausible upper limit for realistic models of the near shore zone (at least for the time
479 being). In the following, the case $h = 50m$ is the subject of greater attention.

480 The model errors are generally similar to those predicted by the ACM linear theory
481 (Figure 4a and Figure 4c). A notable difference is that errors tend to zero when N increases
482 in the case of the theory but not in the case of the model. This is explained by additional
483 sources of error, of numerical origin, in the case of the model. These numerical errors are
484 more important for small periods. For example, for a period of 6s, the residual error for large
485 values of N is around 3% for $h = 50m$ and around 2% for $h = 10m$ (Figure 4a and Figure 4b).
486 The agreement between the model and the ACM linear theory is less good for $h = 10m$,
487 especially for a period of 6s (Figure 4b and Figure 4d). The relative predominance of
488 numerical errors is here related to the decrease of the wavelength caused by the decrease
489 of h . For a period of 6s and $h=10m$, the wavelength is indeed around 48m, i.e. less than 10
490 grid points while the wavelength is around 56m i.e. more than 11 points when $h = 50m$.
491 Actually, when h decreases, causing the wavelength to decrease, the resolution of the
492 horizontal grid eventually becomes insufficient to represent the shortest waves, unless wave
493 breaking occurs before this critical situation.

494 Model errors are also sensitive to vertical resolution. The accuracy of the vertical
495 profile of q and current depends on the number of vertical levels. The shortest wavelengths
496 are particularly sensitive to this error because the vertical profile of q is more non-linear and
497 is established on a smaller depth. Figure 5 shows that for the 6s period, the relative error is
498 much smaller with 80 levels than with 10 or 20. Using more vertical levels reduces the
499 residual error (but does not completely eliminate it). The error levels obtained with 40 levels
500 or 80 levels are however equivalent. For larger periods (results not shown), the sensitivity of
501 the error to the vertical resolution is smaller, plausibly because the vertical profile of the
502 fields, whose characteristic scale of decay is related to the wavelength, is less sheared.



503

504 *Figure 5: relative error on the wavelength (vertical axis) as a function of N (horizontal axis). $h=50m$.*

505 *$dx = 5m$. The horizontal dashed black line indicates a relative error of -1.5%. The period is 6s. Each*

506 *curve corresponds to a different number of vertical levels. From top to bottom: 80 regular levels*

507 *(magenta), 40 regular levels (dashed bold black line), 20 regular levels (blue), 10 levels tightened*

508 *near the surface (green), 10 regular levels (red).*

509

510 The “minimum” error level, around 1.5% in [Figure 5](#) (case 80 levels, $N=20$), is attributable to

511 the time-stepping method itself and no longer depends on the non-hydrostatic aspects. This

512 aspect of the error can be examined in the hydrostatic model by re-invoking the simple

513 assumptions we made in section 2.1. Combining the equation (1) (now without term q) and

514 (3) the surface elevation is given by:

515

516
$$\frac{\partial^2 \eta}{\partial t^2} = c^2 \frac{\partial^2 \eta}{\partial x^2} \quad (30)$$

517

518 Given the numerical schemes used by our model, the error is respectively of the order of

519
$$\frac{dt^2}{12} \frac{\partial^4 \eta}{\partial t^4} \approx \frac{dt^2}{12} \omega^4 \eta \quad \text{and} \quad c^2 \frac{dx^2}{12} \frac{\partial^4 \eta}{\partial x^4} \approx c^2 \frac{dx^2}{12} k^4 \eta$$
 for the left- and right-hand sides of (30). These

520 errors are estimated from the first terms of a Taylor expansion (APPENDIX C). The

521 compensation of temporal and spatial discretization errors is a characteristic of this type of

522 discrete equation (Lemarié et al, 2015, page 127 paragraph 2). Here we see that the two

523 above errors are compensated when the time step is at its theoretical maximum, i.e.

524 $dt = dx/c$ (with $c = \omega/k$). When the time step is significantly smaller (consequence of the

525 increase of N) the time-dependent error becomes negligible and the error is reduced to the

526 error of the right-hand side, $c^2 \frac{dx^2}{12} \frac{\partial^4 \eta}{\partial x^4}$, also equivalent to $-c^2 \frac{dx^2}{12} k^2 \frac{\partial^2 \eta}{\partial x^2}$, and then the

527 discretization of the (30) equation tends to behave like (APPENDIX C):

528

529
$$\frac{\partial^2 \eta}{\partial t^2} \approx c^2 \frac{\partial^2 \eta}{\partial x^2} - c^2 \frac{dx^2}{12} k^2 \frac{\partial^2 \eta}{\partial x^2} + \dots \quad (31)$$

530

531 so that the modelled phase speed approaches $c \sqrt{1 - \frac{dx^2}{12} k^2} \approx c \left(1 - \frac{dx^2}{24} k^2\right)$. The relative

532 error on the phase speed is therefore of the order of $\frac{dx^2}{24} k^2 = \frac{(2\pi/n)^2}{24}$ where n is the number

533 of grid points per wavelength. For the shortest wavelengths considered (for which n is

534 around 10), the relative error on c is therefore of the order of 1.5%. Given that the period is

535 imposed by the forcing, this level of error is therefore the one expected for the modelled

536 wavelength and, in fact, it corresponds fairly well to the residual error for $N=20$ and 80 levels

537 (see Fig. 5).

538 In summary, the accuracy of the dispersion properties increases significantly with N

539 until ACM-related errors become small compared to the other error sources mainly the

540 vertical resolution and the order of precision of the numerical schemes used to calculate

541 spatial and temporal derivatives. The determination of N would lead to choosing N around 14
542 in the case of the experiment considered. Another way to choose N is to define an
543 "acceptable" precision level on the dispersion properties, depending on the period of the
544 simulated waves. For example, a relative error of 3% is obtained for $N > 7$ for a period of 8s,
545 $N > 5$ for a period of 10s, etc...

546

547 *4.2 Improved accuracy (apart from increasing N)*

548

549 *Distribution of vertical levels*

550

551 The previous paragraph shows that the accuracy decreases appreciably with the
552 wave period. At the shortest periods, accuracy is more sensitive to vertical resolution.
553 Increasing the number of vertical levels is an obvious but expensive way to reduce this
554 second source of error. Modifying the vertical distribution of levels without changing their
555 number is an alternative that allows a significant improvement in accuracy at small periods.
556 In the case of the 6s period, [Figure 5](#) shows that 10 irregularly distributed levels (see Table
557 1) provide a much higher accuracy than 10 equidistant levels, and makes it comparable to
558 the precision obtained with 20 equidistant levels. The vertical distribution proposed here is
559 such that the accuracy is also improved or maintained for the other periods considered
560 (results not shown).

561

levels	Relative thickness dz/h
10	0.03852
9	0.04623
8	0.05547
7	0.06657
6	0.07988

5	0.09586
4	0.11503
3	0.13803
2	0.16564
1	0.19877

562 *Table 1: Thickness of the ten layers (1 corresponds to the bottom) as a fraction of the water depth.*
563

564 It should be noted that, in a realistic domain, the generalized sigma coordinate makes it
565 possible to adapt the vertical distribution to the bathymetry. For example, in areas where
566 bathymetry is low relative to wave wavelength, the vertical profile of current and pressure is
567 less sheared and a more regular distribution of the levels is preferable to the irregular
568 distribution of Table 1. Given the positive influence of increasing vertical resolution on
569 accuracy, the increase in vertical resolution that results from the decrease in bathymetry in
570 the sigma formulation leads to a better representation of dispersion properties when
571 approaching the coast.

572

573 *Influence of horizontal resolution*

574

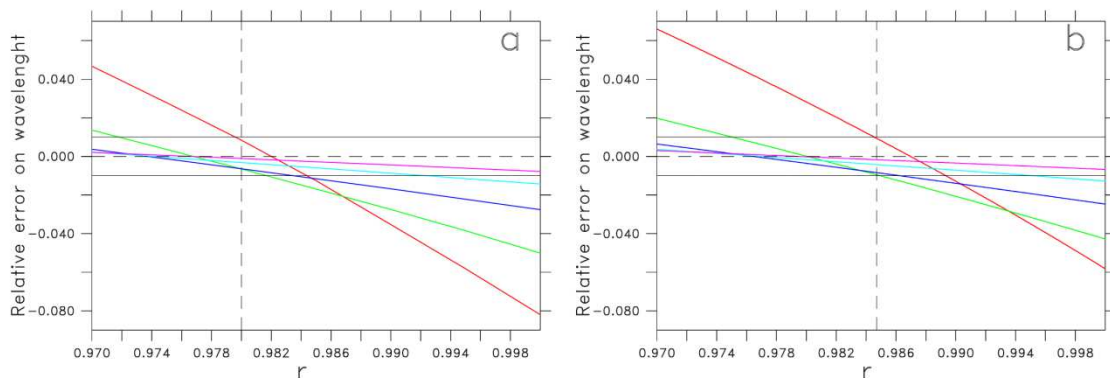
575 Increasing the horizontal resolution (without changing the other parameters,
576 especially N) leads logically to decrease the level of error, especially at short periods.
577 Significantly increasing the horizontal resolution has a real but limited impact on the
578 accuracy because of other sources of error such as the lack of vertical resolution. The period
579 6s is more critical than the other periods tested because, as noted above, the number of grid
580 points per wavelength is particularly low. Doubling the resolution allows about 22 grid points
581 per wavelength (for $h=50m$). Fig. 4 shows that a relative error <3% is obtained with $N > 10$ for
582 a horizontal resolution of 2.5m, whereas this same level of error requires $N > 14$ for a
583 horizontal resolution of 5m.

584

585 *Tuning the non hydrostatic pressure gradient*

586

587 A modification of the pressure gradient scheme is now proposed to use moderate N
 588 values while maintaining an acceptable level of accuracy on dispersion properties. We
 589 consider values of N around 5. The proposed modification is suggested by the observation
 590 that the error on the wavelength is systematically negative (Figs 4 and 5). This is equivalent
 591 to the fact that the modelled phase speed is systematically lower than the theoretical phase
 592 speed. In other words, the non-hydrostatic effect excessively decreases the phase speed.
 593 This conjecture can be interpreted as an overestimation of the non-hydrostatic component of
 594 the pressure gradient in agreement with the conclusions drawn from the analytical solution of
 595 the linearized ACM equations (section 3, Figure 1). The proposed improvement consists in
 596 moderating the non hydrostatic pressure gradient by multiplying the latter by a constant r
 597 slightly less than 1 (see the non-hydrostatic pressure gradient terms in equations (7) and
 598 (8)).



599 *Figure 6: Relative error on the wavelength as a function of r . Model (a) and ACM linear theory (b).*
 600 *$h=50m$. $N = 5$. Horizontal black lines indicate a relative error of + or - 1%. Each curve corresponds*
 601 *to a period: 14s (magenta), 12s (cyan), 10s (blue), 8s (green), 6s (red). The dashed vertical line*
 602 *corresponds to $r = 0.98$ (a) and $r=0.9845$ (b) for which all relative errors are between +/- 1%*
 603

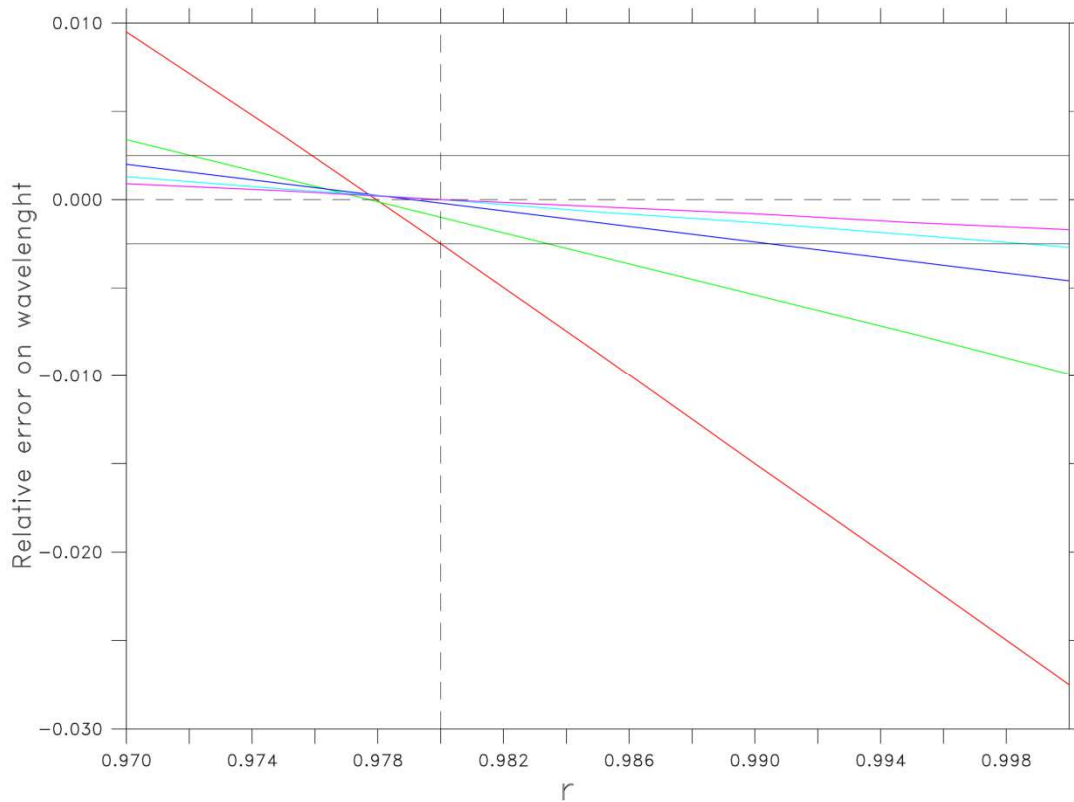
604

605

606 Fig. 6a, obtained with $N=5$ ($dt = 0.032s$), shows that the precision is improved when r
607 decreases to a certain level below which the sign of the error is reversed (becoming positive)
608 and the error increases again. As expected from the ACM linear theory, the value of r that
609 exactly cancels the error is not the same depending on the period. It is around $r=0.982$ for
610 the 6s period and smaller for the other periods. The general behaviour is nevertheless quite
611 similar for all the periods and one can identify a unique value of r which makes it possible to
612 reduce the error below 1% for all the periods (Figure 6a, $r=0.98$), which corresponds to a
613 very significant reduction of the error, especially for small periods (error of 8% and 5% for
614 periods of 8s and 6s respectively, with $r=1$). The general behaviour of the model is in good
615 agreement with the analytical solution (Figure 6b). However, since the model has other
616 sources of errors than those of the theoretical model, Figures 6a and 6b are not strictly the
617 same and the best compromise for the value of r would be slightly larger according to (24),
618 around 0.984 (Figure 6b). Although the theoretical model could certainly be used for a
619 default setting of r , Figure 6a shows that errors can be further reduced with an empirical
620 setting. This numerical estimate of the best compromise on r is therefore used in the
621 following.

622 As pointed out previously, a realistic numerical domain is characterized by variable
623 bathymetry. As 50m should be an upper limit of a near shore zone model in our future
624 applications, we now verify that the value $r=0.98$, which reduces the error below 1% for all
625 periods when $h=50m$, remains relevant for lower values of the water depth. These tests are
626 done keeping the same time step ($dt=0.032s$) and $N=5$. Figure 7, obtained for $h=20m$, shows
627 a precision greater than the simulation with $h=50m$, under the combined effect of the
628 increase of the vertical resolution (the same number of vertical levels distributed over a
629 shallower water column) and also the decrease in the non-hydrostatic effect caused by the
630 decrease in the ratio between the horizontal scale and the vertical scale. If Fig. 7 suggests
631 that the best value of r would be around 0.978 (the minimum relative error is indeed close to
632 this value for most of the periods considered), the proposed value of 0.98 for $h=50m$ remains

633 relevant for shallower depths because it reduces the relative error associated with the
634 different periods between -0.25% and 0%.



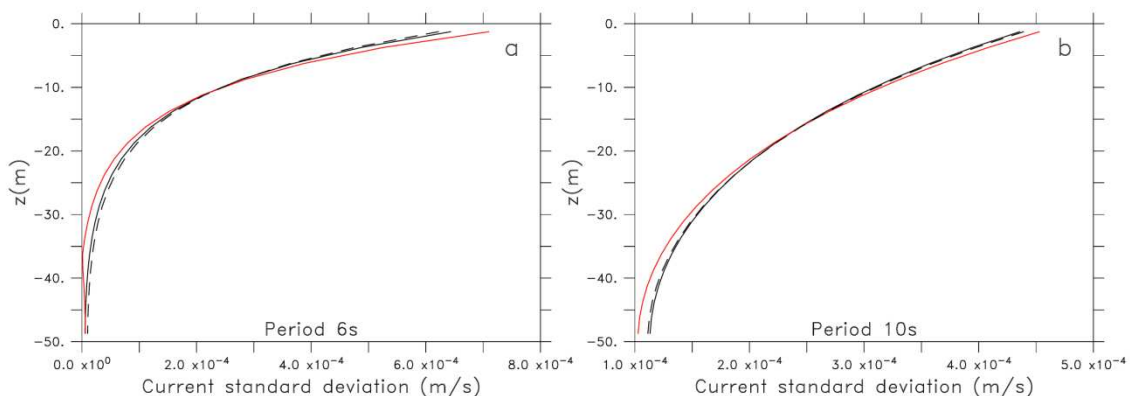
635
636 *Figure 7: as Figure 6a but $h=20m$. The 2 horizontal black lines indicate a relative error of + or -*
637 *0.25%. The dotted vertical line corresponds to $r = 0.98$ for which all relative errors are between -*
638 *0.25% and 0%.*

639

640

641 Note finally that the choice of the 50m value as the maximum value of the bathymetry
642 is somehow arbitrary. There are certainly other ways of defining the offshore limit of the near
643 shore zone, such as the depth at which the waves are modified by the seabed. In this case,
644 a maximum value based on the relative depth, kh , may be preferable.

645 The ability to strongly reduce, or even cancel, the error via the r parameter means
646 that this parameter can be used to correct errors beyond the single error caused by the ACM
647 method. The errors associated with the vertical discretization or the time-stepping scheme
648 can therefore be compensated by this method. We thus examine the possible undesirable
649 consequences of this compensating effect on other important properties of wave physics
650 especially since, according to the theoretical model, the cancellation of the errors on the
651 current and the relation of dispersion is not obtained strictly with the same value of r (e.g.
652 (28) and (29)). Recall also that the shape of the vertical profile of the current is of particular
653 interest, since the intensity of the current near the bottom is crucial for the determination of
654 the bottom friction, the resuspension of sediments near the bottom, the transport of sand
655 (among others). Figure 8a shows that for the period 6s, $r=0.98$ leads to a vertical profile of
656 the current more accurate than with $r=1$ (the latter nevertheless correctly reproduces the
657 vertical shear), the value $r=0.986$ being the one that would lead to a profile closest to the
658 profile predicted by the linear non-hydrostatic incompressible theory. A similar conclusion is
659 made for the period 10s (Figure 8b) for $r=0.976$. The fact that a single value of r can both
660 reduce the error on the dispersion relation and the current is finally consistent with Figure 3
661 which shows that the values of r cancelling these two types of error are actually very close.
662



663
664 *Figure 8: Standard deviation of the horizontal component of the current (m / s) as a function of the*
665 *depth (m) calculated over the last 4 simulated periods at a distance of 625m (125 points) from the*

666 *incoming boundary. The period is 6s (a) or 10s (b). $h=50m$, 20 vertical levels, $dx = 5m$, $N = 5$, $r = 1$*
667 *(red line), $r = 0.98$ (black dotted line), theoretical profile from the incompressible linear theory*
668 *(continuous black line). For the sake of clarity the profiles corresponding to $r = 0.986$ (period 6s) and*
669 *to $r = 0.976$ (periode 10s) are not shown because they merge with the theoretical profiles.*

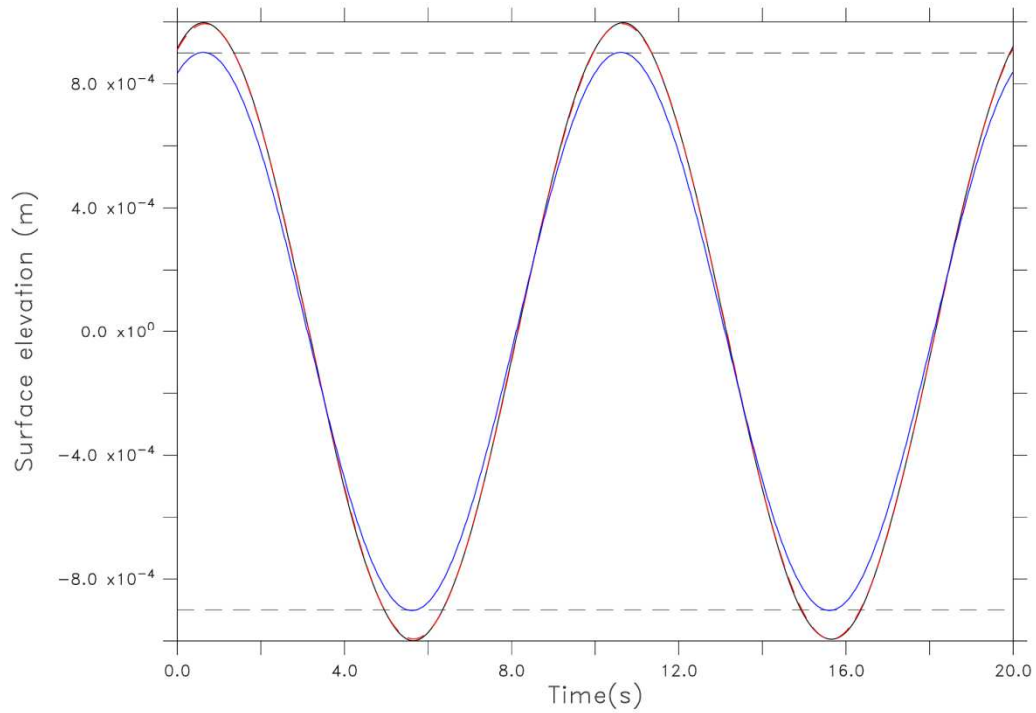
670
671

672 **4.3 Test case with bi-periodic domain**

673

674 We are now replacing open and closed boundary conditions at both ends of the
675 domain in the propagation direction by periodic conditions. The interest of this bi-periodic
676 domain is that it avoids reflections at the boundaries that could degrade the results. The
677 simulations can therefore be long, which is of interest for testing the stability of calculations
678 in the long term. The depth is 50m. The domain has 510 points in the direction of
679 propagation corresponding to a whole number of wavelengths, here 17, for a wavelength of
680 150m, a theoretical period close to 10s and a phase speed close to 15m/s. The fields are
681 initialized from the linear theory. The amplitude of the surface elevation is small (1 mm) to
682 remain within the framework of the linear theory. Nonlinear dissipation forces such as friction
683 (using a quadratic parameterization) or breaking are therefore negligible. In this particular
684 case, the Laplacian temporal filter derived from Marsaleix et al. (2012), used in the equations
685 for u , v , q to suppress the numerical mode, is the main source of dissipation. The following
686 test quantifies its adverse effect on the long-term physical mode. [Figure 9](#) shows the
687 amplitude of the surface elevation at different times. Given the value of the phase speed, a
688 distance of the order of 10km (cross shore size of realistic domains that we plan to use with
689 this model) is covered in about ten minutes. [Figure 9](#) shows that the attenuation is negligible
690 over such a short time duration. An attenuation of 10% would require at least 6 hours, during
691 which the waves would travel a distance of about 300 km. [In our future realistic applications,](#)
692 [the open boundary condition will not be located so far from the coast. The cross-shore](#)
693 [domain dimension should be at least an order of magnitude lower, so this numerical](#)

694 attenuation should be less than 1%, in other words small compared to the expected erosion
695 induced by bottom friction, turbulence or wave breaking.
696



697
698 *Figure 9: Surface elevation (m) as a function of time (s) at the beginning of the simulation (red*
699 *curve), after 10mn of simulation (black dotted curve), after 6 hours of simulation (blue curve).*
700 *$h=50m$, $dx = 5m$, 20 vertical levels, $N = 5$, $r = 0.98$. The 2 horizontal black dotted lines indicate an*
701 *attenuation of the initial amplitude of 10%*

702

703

704 **4.4 The case of a linear slope beach**

705

706 The Hamilton and Ebersole laboratory experiment (Hamilton and Ebersole 2001
707 hereafter HE01, Svendsen et al 2003) focuses on the propagation of waves over a uniform
708 linear slope beach, their breaking, and the alongshore current establishment. This case test
709 is of particular interest to us to assess the performances of the model on the important
710 question of the parametrization of wave breaking. Incoming waves are monochromatic, with
711 a period of 2.5s (TEST 6N in HE01). The amplitude of the excited waves at the open
712 boundary is adjusted to obtain a wave height corresponding to the conditions of TEST 6N,
713 namely 0.19m at the most offshore measurement points (see the observation at 3 meters
714 from the incoming boundary on Fig. 10). The direction of propagation is 10° from the
715 direction normal to the beach. A description of the basin and its bathymetry is given in
716 Svendsen et al. (2003) (see also Fig. 10). The particularity of the basin lies in its pumping
717 and recirculation system made of 20 pumps that allow having periodic conditions on the
718 lateral boundaries. In our simulation, incoming waves are specified from the linear theory at
719 the offshore boundary. Periodic boundary conditions are applied at the lateral boundaries of
720 the model. The dimension of the domain in the direction parallel to the beach is consistent
721 with the condition of periodicity and the wave propagation direction of 10° in the deep part of
722 the basin. The horizontal resolution is 0.1m and the grid has 10 vertical levels. The
723 dimension in the cross-shore direction is 18m and the deepest bathymetry, offshore, is
724 0.66m. The maximum wavelength, in the deep part of the basin, is of the order of 6m. A
725 steady state is reached after about 150s. The results presented are obtained at the end of a
726 simulation of 500s. The roughness of the bottom corresponding to this experiment is a priori
727 not mentioned by its authors. A roughness length of $3 \times 10^{-5}m$ was empirically fixed in our
728 model in order to obtain a satisfactory agreement with the vertical profile of the measured
729 alongshore current.

730 The basin dimensions are small compared to a real case. If the ratio of the horizontal scale
731 on vertical scale is used to deduce the characteristics that this experiment would have with
732 dimensions 50 times larger, close to the dimensions of the test cases presented in the
733 previous section, we obtain a horizontal resolution of 5m, a maximum depth of 30m, a

734 maximum wavelength of the order of 300m and a period of 125s. We are thus in conditions
 735 for which the problems of accuracy examined in the preceding sections are minor and make
 736 it possible to use the ACM method with a small value of N and a coefficient of reduction of
 737 the gradient of q close to one. In practice we use $N=4$, $r=1$ (as mentioned previously, we
 738 actually chose this test case for the wave breaking issue rather than the non-hydrostatic
 739 specificities discussed in the previous test case).

740 Wave breaking is parameterized through the horizontal diffusion of the momentum
 741 (13). The determination of the mixing coefficient, ν_b , is an important aspect of this
 742 parameterization. Before going into the details of its calculation, we examine the order of
 743 magnitude necessary for the decay of the waves inside the breaking zone. To do this, we
 744 consider an energy balance between the gradient of the potential energy flux $\frac{\partial(g u \eta)}{\partial x}$ and
 745 dissipation due to horizontal diffusion $-\nu_b \left(\frac{\partial u}{\partial x}\right)^2$ (for the sake of clarity we limit ourselves to
 746 unidirectional propagation along the Ox axis). We hypothesize that within the wave breaking
 747 zone the wave height is proportional to the water depth (Miche, 1944):

748

$$749 \quad \frac{H}{h} = \gamma \quad (32)$$

750

751 where H is the wave height. We consider here that the parameter γ is a constant of the order
 752 of 0.8 (it can nevertheless be noted that the expression of γ can be more sophisticated, as in
 753 Guérin et al. 2018). For convenience (and considering that shallow depths, where breaking
 754 mostly occurs, allow this approximation) the hypothesis of hydrostatic equilibrium is made in
 755 the following reasoning (although the simulations presented are still non-hydrostatic). We
 756 thus consider that the current and the surface level are connected to each other according to
 757 $u = \frac{g}{c} \eta$ where $c = \sqrt{gh}$. It is finally assumed that the fields have a sinusoidal behaviour and
 758 that the wave amplitude η_0 satisfies (32) (ie $\frac{2\eta_0}{h} = \gamma$). Averaging over a period of waves, the
 759 gradient of the potential energy flux is (APPENDIX D):

760

761

762
$$\frac{\partial(gu\eta)}{\partial x} = g^{3/2}\gamma^2 \frac{3}{16} h^{1/2} \frac{\partial h}{\partial x} \quad (33)$$

763

764 and dissipation due to horizontal mixing is

765

766
$$\varepsilon_b = -\nu_b \frac{1}{8} \left(\frac{kg\gamma h}{c} \right)^2 \quad (34)$$

767

768 The equilibrium of (33) and (34) leads to an estimation of the average of the mixing
769 coefficient over a period of waves:

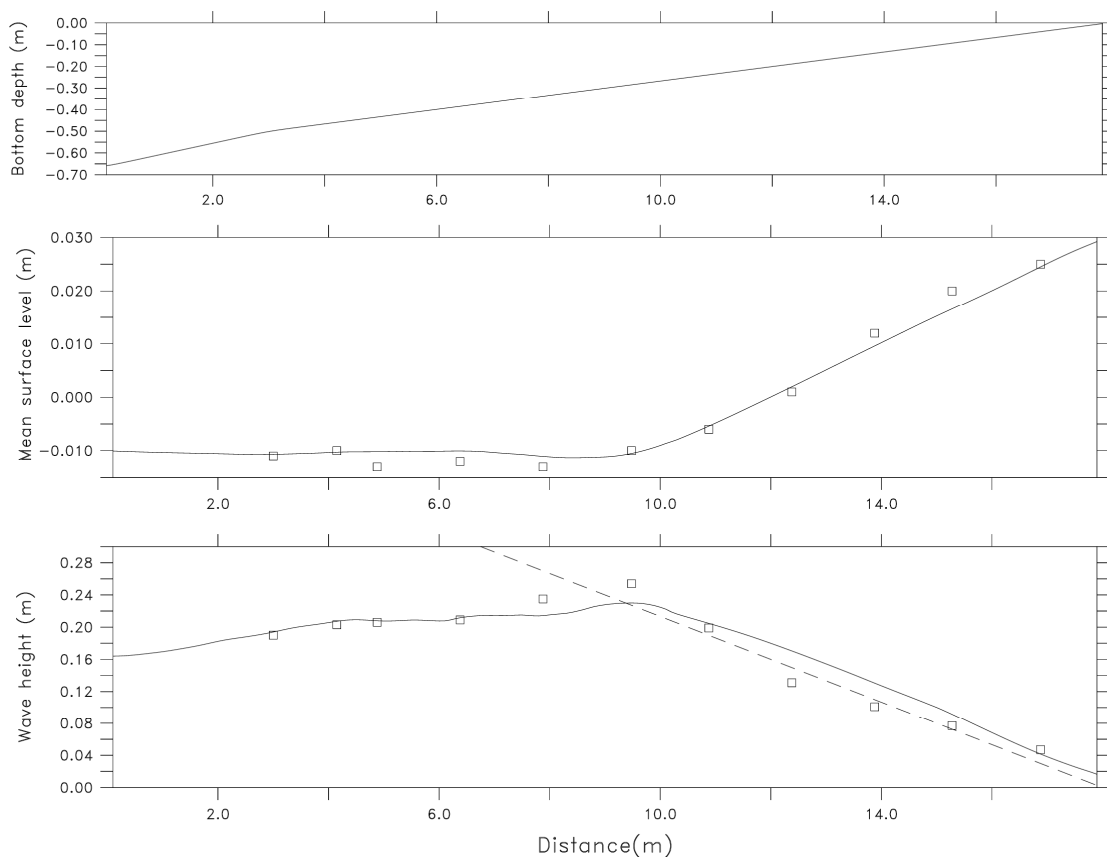
770

771
$$\langle \nu_b \rangle = \frac{3}{8} g^{3/2} h^{1/2} \frac{\partial h}{\partial x} \left(\frac{T}{\pi} \right)^2 \quad (35)$$

772

773 The latter increases with the slope of the bathymetry and vanishes when the thickness of the
774 water column is zero. The expression (35) is only an intermediate step towards a more
775 complete formulation taking into account a triggering criterion based on the analysis of the
776 instantaneous modelled fields. But before addressing this aspect, a preliminary experiment
777 is carried out to test the relevance of the order of magnitude given by (35). Practically (35) is
778 used as the value of the horizontal diffusion coefficient in (13) inside the wave breaking
779 zone. The latter is arbitrarily defined from a threshold on bathymetry ($h < 0.28m$) deduced from
780 observations of wave heights (HE01). In the pre-breaking zone ($h > 0.28m$) $\nu_b = 0$. [Figure 10](#)
781 shows the simulated wave height and mean elevation, and the corresponding observations
782 of HE01. As the laboratory experiment, the simulation lasts 500s. The surface height is
783 averaged over the last 50 seconds of the simulation. The wave height is calculated from the
784 difference between the maximum and minimum values of the surface level over the last 50
785 seconds of simulation. The agreement is satisfactory. The wave breaking trigger point is

786 unsurprisingly well positioned since it is imposed by the criterion $h < 0.28m$. The wave height
 787 is slightly overestimated in the breaking zone but the slope of decrease is parallel to that of
 788 the theoretical decay $\frac{2\eta_0}{h} = \gamma = 0.8$ (dotted line in Fig. 10). It should be noted that several
 789 simulations were performed by increasing or decreasing slightly the value of $\langle v_b \rangle$ and
 790 that Figure 10 corresponds to a 5% increase in the value predicted by (35).
 791



792
 793 **Figure 10.** Top: Bottom depth (m). Middle: mean surface levels (m). Solid line: simulation. Squares:
 794 longshore-averaged observations from HE01. Bottom: wave height (m). Solid line: simulation.
 795 Squares: longshore-averaged observations from HE01. Dashed line: $0.8h$. Horizontal axis: cross-
 796 shore distance from incoming boundary in meters.

797

798

799 *Breaking criterion*

800

801 Practically (35) is not really appropriate because it requires to arbitrarily specify the
802 location of the onset of breaking. In realistic case, the breaking point of the breaking wave
803 varies over time, in particular according to the characteristics of the waves and more
804 generally according to the surrounding hydrodynamic conditions. An extension of (35) taking
805 into account the instantaneous fields is therefore proposed:

806

$$807 \quad \nu_b = \langle \nu_b \rangle f_b \quad (36)$$

808

809 Where ν_b is the instantaneous coefficient, $\langle \nu_b \rangle$ is the average coefficient (35) and f_b is a
810 function that triggers the wave breaking according to the instantaneous fields. The average
811 of f_b over a period of wave is expected to be close to 1 so that the viscosity is on average
812 close to $\langle \nu_b \rangle$. One consequence of this property is that ν_b can be momentarily very high if
813 f_b is negligible over a large fraction of the wave period (so that the average of ν_b stays close
814 to $\langle \nu_b \rangle$). Many authors use the ratio of the wave height to the water depth (the γ constant
815 (32)) as breaking criterion (Rusu and Soares, 2012). Others use criteria based on the
816 horizontal gradient of the modelled fields (Lynett, 2006). For example, Zijlema et al (2011)
817 propose to formulate eddy viscosity from Prandtl's length and a turbulence equilibrium
818 hypothesis which in practice links eddy viscosity to the horizontal gradient of velocities (see
819 their equation 12). Roeber and Cheung (2012) also use the velocity gradient (see their
820 equation 70) but in an approach that is more akin to a criterion on the Froude number, with
821 \sqrt{gh} as an approximation of the phase speed. These authors emphasize that this criterion
822 has the particularity to be more influential in areas where the slope of the waves is important
823 in contrast to the H/h criterion which favours the wave crests. The criterion on the gradient
824 is therefore in principle influencing a larger proportion of the breaking zone. From the point of

825 view of (36), an approach of this type should lead f_b to act on a larger time interval and thus
826 limit the maximum values of v_b . On the other hand, a criterion on the wave crest should lead
827 f_b to be small over a large fraction of the wave period, with the aforementioned consequence
828 of momentarily strong v_b values. This consideration may be of numerical importance as
829 there is a stability criterion which limits the eddy viscosity value for a given time step (Zijlema
830 et al, 2011). In the particular case of this experiment, we find that a wave breaking criterion
831 based on H/h can cause the eddy viscosity to momentarily exceed the maximum value
832 allowed by the CFL criterion (ie $v_b > v_b^{max} = \frac{1}{4} \frac{dx^2}{dt}$). One possibility of overcoming this
833 problem is either to reduce the time step of the model, or to use a time splitting technique
834 with a smaller time step for the calculation of the wave breaking without impacting the time
835 step of the other equations of the model. From a numerical point of view, the approach
836 proposed by Roeber and Cheung (2012) is interesting because their parameterization of the
837 wave breaking should act on a longer duration, limiting the maximum values of the breaking
838 viscosity. We choose this approach, mainly for the aforementioned numerical issues, but we
839 propose to add a modification to that method in order to extend the influence of the breaking
840 criterion to an even greater proportion of the breaking zone. This is arguably questionable
841 from the point of view of the realism of the process (Kennedy et al, 2000) but it is an
842 interesting option considering the numerical aspects mentioned above. More specifically, our
843 objective is to avoid reducing the time step because of a too restrictive stability condition
844 related to the wave breaking scheme.

845 The triggering criterion for wave breaking is inspired from Roeber and Cheung (2012)
846 but is modified to be active both on the wave crest and between crests. This criterion
847 considers both velocities and their horizontal gradient. The velocity gradient is scaled by the
848 wavenumber so that the two quantities have the same order of magnitude. A wave breaking
849 criterion is then given by the ratio of the sum of these fields to the hydrostatic phase speed
850 (for simplicity the following formula is given in the case of unidirectional propagation):

851

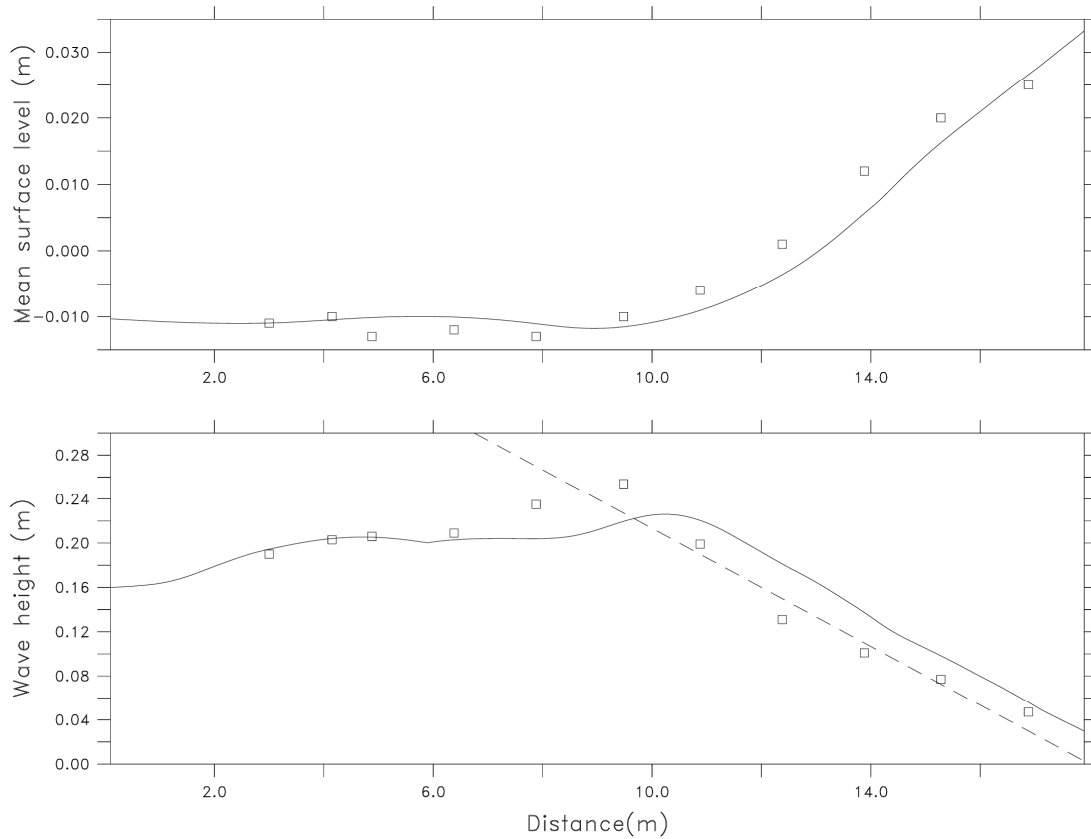
852
$$f_b = c_1 \left[\frac{u_s^2 + \left(\frac{1}{k} \frac{\partial u_s}{\partial x} \right)^2}{gh} \right]^{n/2} \quad (37)$$

853

854 Where u_s is the surface current and k is the wavenumber fixed a priori according to the
855 peak period prescribed at the open boundary. The constant c_1 is determined empirically:
856 ideally, its role is to allow the average value of f_b to be of the order of unity over a period of
857 waves (so that the eddy viscosity is on average close to (35)). It may be noted that in the
858 idealized framework of the linear theory (where the current would be of the form $u_0 \cos(\omega t +$
859 $kx)$) the term in the numerator of (37) would simply be u_0 , independent of time, and, in a
860 breaking situation characterized by a current of an order of magnitude comparable to that of
861 the phase speed, the constant c_1 would simply be of the order of (35). The exponent, n , is
862 used to adjust the selectivity of the criterion. It is in particular chosen so that f_b tends more
863 rapidly towards 0 upstream of the breaking zone. The simulations presented in the following
864 use $n=2$.

865

866



867

868 *Figure 11. As Figure 10 but eddy viscosity calculated with (36) and (37). Top: mean surface level*
 869 *(m). Bottom: wave height (m). Dashed line: $0.8h$.*

870

871

872 **Figure 11** corresponds to an eddy viscosity calculated with (36) and (37) instead of (35) with
 873 the arbitrary hypothesis on the depth of the breaking onset (the other parameters being
 874 identical to those of the previous simulation). It is comparable to **Fig. 10**. The main difference
 875 is in the behaviour within the breaking zone where the curves are a little less linear in the
 876 case of **Fig. 11**, as a consequence of the non-linear character of (36) and (37). Although the
 877 simulation is slightly less close to the observation in the case of **Fig. 11**, we prefer to use
 878 (36) and (37), whose formulation is more general rather than (35) which suffers from its
 879 arbitrary definition of the trigger point of breaking.

880

881 *Taking into account the breaking in the turbulent closure scheme*

882

883 The turbulence scheme used here is the k-epsilon scheme (Rodi, 1987). A wave-
884 related turbulence generation term may be taken into account when the circulation model is
885 coupled to a phase-averaged wave model (Michaud et al, 2012). In the present case, this
886 term is not taken into account because the explicit modelling of the waves leads naturally to
887 a significant production of turbulent kinetic energy (TKE) through the vertical shear of the
888 current. The relevance of adding an additional production term to represent the assumed
889 increase in turbulence in the breaking zone is an open question (Feddersen and Trowbridge,
890 2005) and is therefore examined here. The HE01 experience provides the opportunity to
891 examine this point by providing measurements of the residual onshore current at different
892 depths and at different distances from the edge of the basin. Here, an additional production
893 term, P_{wb} , representing a fraction of the kinetic energy lost by the current via the horizontal
894 mixing associated with the breaking (ie (36), (37)) , is introduced into the TKE equation of
895 the k-eps scheme:

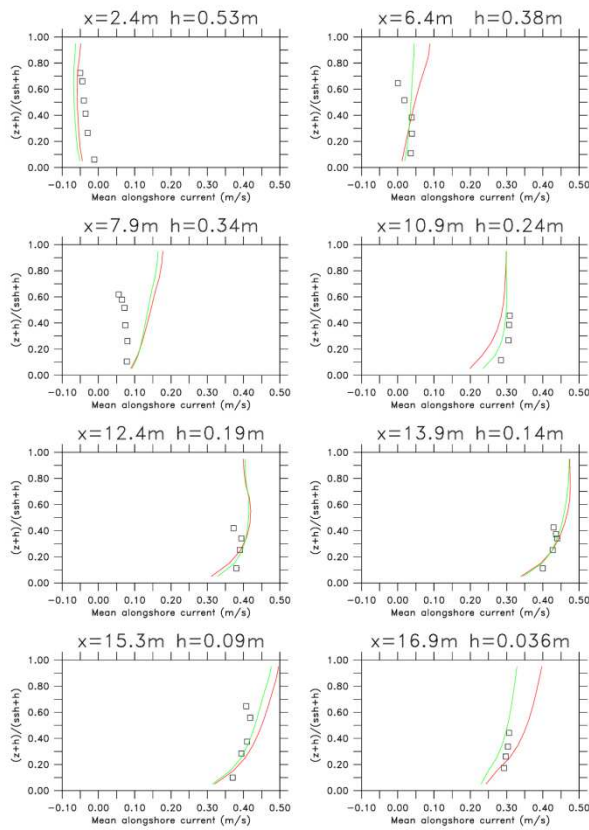
896

897
$$P_{wb} = c_2 \nu_b \left[\left(\frac{\partial u}{\partial x} \right)^2 + \left(\frac{\partial u}{\partial y} \right)^2 + \left(\frac{\partial v}{\partial x} \right)^2 + \left(\frac{\partial v}{\partial y} \right)^2 \right] \quad (38)$$

898

899 Where c_2 is a constant between 0 and 1. Equation (38) implies that a fraction of the breaking
900 energy feeds the vertical mixing. The simulated alongshore residual current is obtained by
901 averaging the alongshore current during the last 50 seconds of the simulation. [Figure 12](#)
902 shows the comparison with the observed current from HE01. Note that the vertical axis has
903 been normalized so that the figure is easily comparable to that of Svendsen et al. 2003 (see
904 their figure 11). Two simulations are made, one with $c_2 = 0$ the other with $c_2 = 0.01$. The two
905 simulations generally give rather satisfactory results with the exception of the current at
906 $x=7.9m$. Looking more closely at [Fig. 12](#), we notice that the simulation taking into account

907 P_{wb} (red lines) gives a better agreement with the observations. The simulation without P_{wb}
 908 ($c_2 = 0$, green lines) shows indeed a current with a greater vertical gradient than that of the
 909 observation, in particular at the points located in the shallowest depths. Increasing the
 910 vertical mixing coefficient associated with P_{wb} reduces the current shear in the breaking
 911 zone. We therefore retain at this stage that this approach can be used to improve turbulence
 912 in the wave breaking zone. However, in the state of our knowledge, the setting of c_2 is
 913 arbitrary and would need to be estimated on other experiments, including in situ data such
 914 as current profiles or more direct observations of turbulence (Costa et al. 2017).



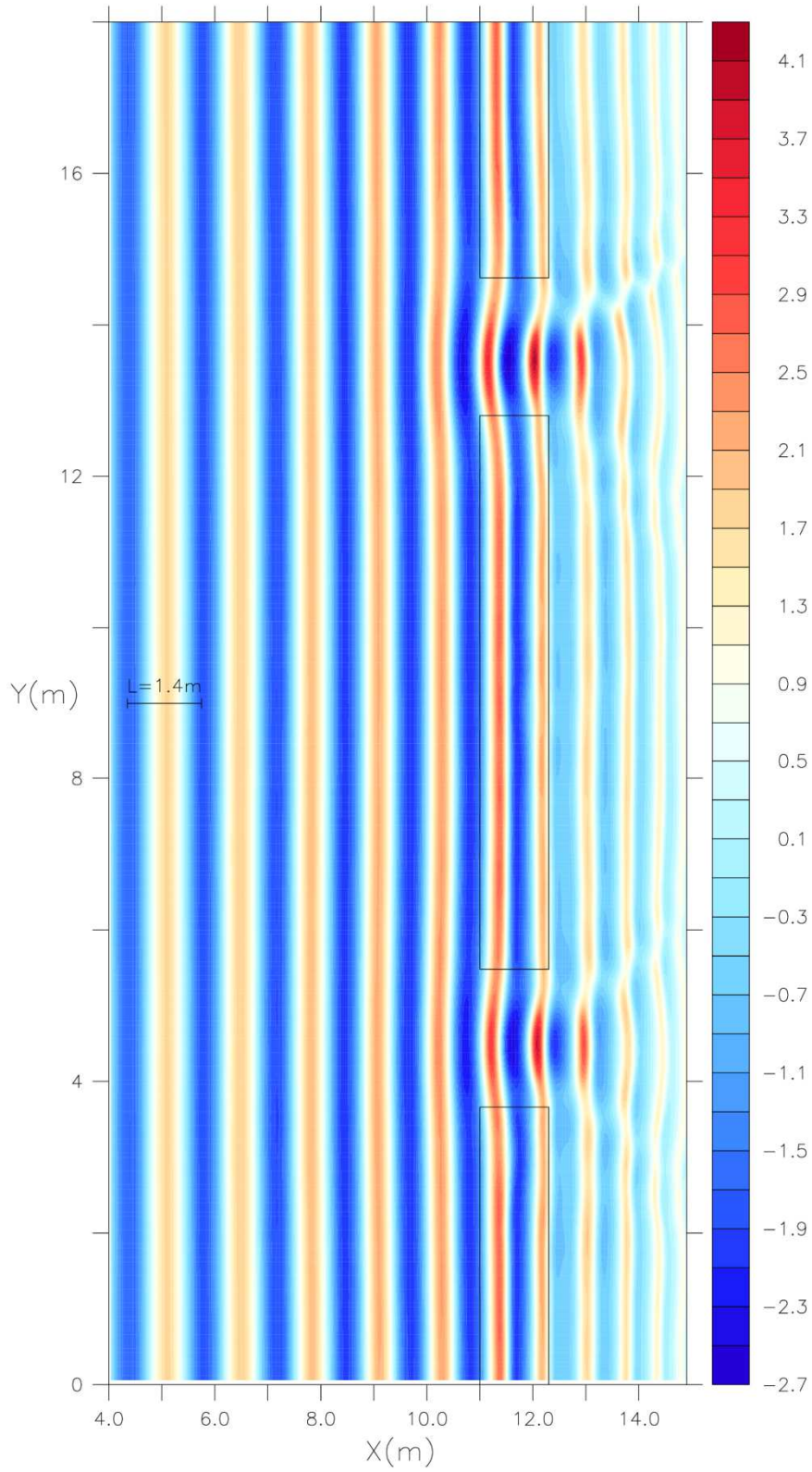
915
 916 *Figure 12. Vertical profile of the measured mean alongshore current (black squares), simulated*
 917 *without the term P_{wb} ($c_2 = 0$, green lines), simulated with the term P_{wb} , $c_2 = 0.01$ (red lines).*
 918 *Vertical axis: normalized depth $\frac{z+h}{\eta+h}$. Horizontal axis: m/s.*

919
 920 **4.5 The case of a barred beach with rip currents**

921

922 The interaction of waves and rip currents is an example of the complexity of possible
923 interactions between current and waves (Weir et al, 2011). The model is now applied to a
924 laboratory experiment describing the propagation of monochromatic waves over a beach
925 with a sandy bar and channels inducing rip currents (Haller et al, 2002, Haas and Svendsen,
926 2002). This experiment has already been simulated with hydrostatic circulation models
927 coupled with a phase-averaged wave model (Haas and Warner, 2009, Haas et al, 2003,
928 Michaud et al., 2012, Bruneau 2009). Like these previous authors, we are interested here in
929 TEST B of Haller et al. (2002). The basin and its bathymetry are described in detail in the
930 aforementioned articles. The dimensions of the basin are approximately 17m (cross-shore
931 direction) by 18m (alongshore direction). The cross-shore slope is 1/30. A bar, located a few
932 meters from the coast, is cut by 2 channels. Ideally, the two channels should have an
933 identical shape and the bathymetry of the entire basin should respect an alongshore
934 symmetry: the central bar is twice as long as the two half-bars touching the side walls and
935 outside the bar the alongshore gradient is supposed to be nil. However, as pointed out by
936 Haas et al. (2003), an important feature of this bathymetry is that it actually has irregularities
937 compared to its idealized design, resulting in dissymmetry of the flow and increasing
938 instability of the currents. The two rip currents that form at the exit of the channels are for
939 example clearly different in their form and their intensity, and their respective temporal
940 variations seem rather decoupled. A bathymetry interpolated from a survey of the wave
941 basin is used here to better respect the real conditions of the experiment. The horizontal
942 resolution is 0.06m and the vertical grid has 10 sigma levels. The time step is 1.1×10^{-2}
943 seconds. Monochromatic waves of period 1s propagate in the direction perpendicular to the
944 coast (Fig. 13). The amplitude of the excited waves at the open boundary is adjusted to
945 obtain a wave height corresponding to the conditions of TEST B, namely about 4.1 cm at the
946 most offshore measurement points (see Fig. 14 around $x=8m$). Their wavelength at the
947 entrance of the domain (where the depth is about 0.38m) is about 1.4m (Fig. 13) in good
948 agreement with the linear non hydrostatic wave theory. It may be noted that the hydrostatic

949 approximation under the same conditions would lead to a wavelength of about 1.9m, ie an
950 overestimation of about 35%.



951

952 *Figure 13. Surface elevation (cm) after 1 minute of simulation. black rectangles: position of bars.*
 953 *Short black line with label: scale of the wavelength at the entrance of the basin. Horizontal axis:*
 954 *cross-shore distance (m) from the wave generator. Vertical axis: alongshore distance (m)*

955

956

957 Consistently with Haas and Svendsen (2002) and Haas et al. (2003), the simulation lasts 30
 958 minutes to highlight the observed temporal variations of rip currents. The wave height is
 959 obtained from the difference between the minimum and maximum of the surface level
 960 obtained over time intervals of 1 second. An average wave height is then calculated by
 961 averaging these values obtained every second over the simulation except the first minute to
 962 avoid the spin-up phase. Table 2 summarizes the characteristics of the numerical grid and
 963 the calculation time. The latter can be roughly extrapolated to more realistic applications
 964 considering that the scale ratio between this simulation and that of a realistic case (with for
 965 example $dx=3m$) is about 50, in other words an area of about 1km x 1km and a simulation
 966 duration of about 1 day.

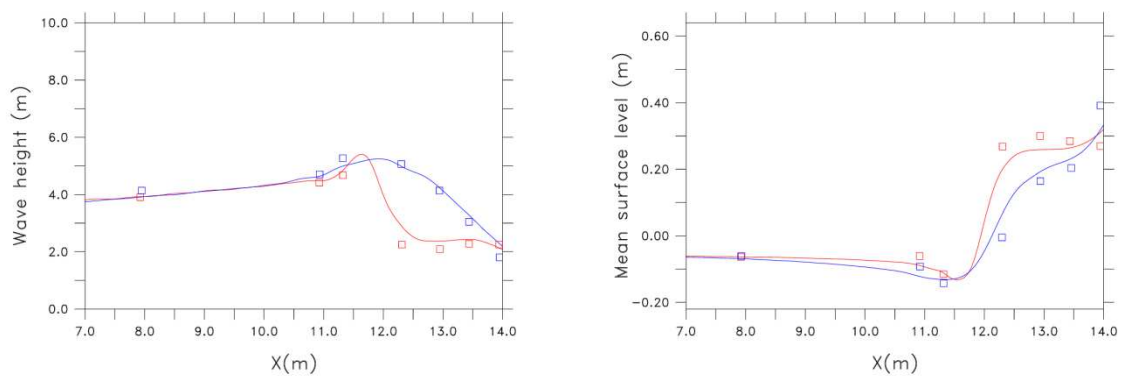
967

Number of grid points	300 x 284 x 10
Horizontal resolution	0.06m
Horizontal size of the domain	18m x 17m
Parallel calculation	72 cores
Duration of the simulation	30 minutes
Number of iterations	1 600 000
Computing time	10h

968 *Table 2: grid specificities and computing time on the OCCIGEN supercomputer administered by*
 969 *CINES (<https://www.cines.fr>)*

970

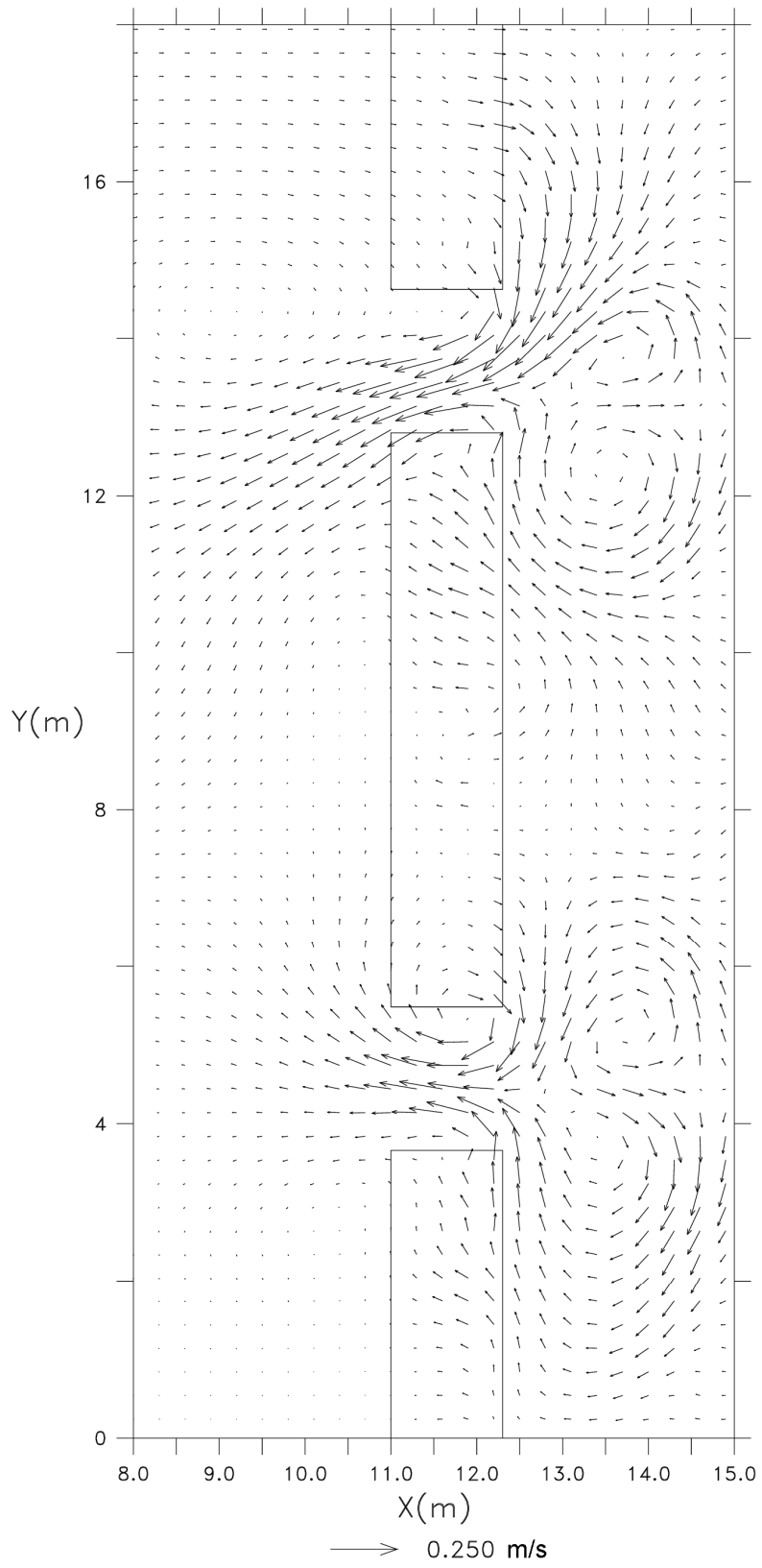
971 The wave height and mean surface height calculated by the model are compared to
972 the observations of the TEST B case (Figures 6 and 16 of Haller et al, 2002). The wave
973 height first increases slowly towards the coast, then increases sharply when the waves
974 arrive above the bar (Figure 14). The breaking conditions are quickly reached and once the
975 bar crossed, the wave height is much lower and relatively constant (Figures 13 and 14).
976



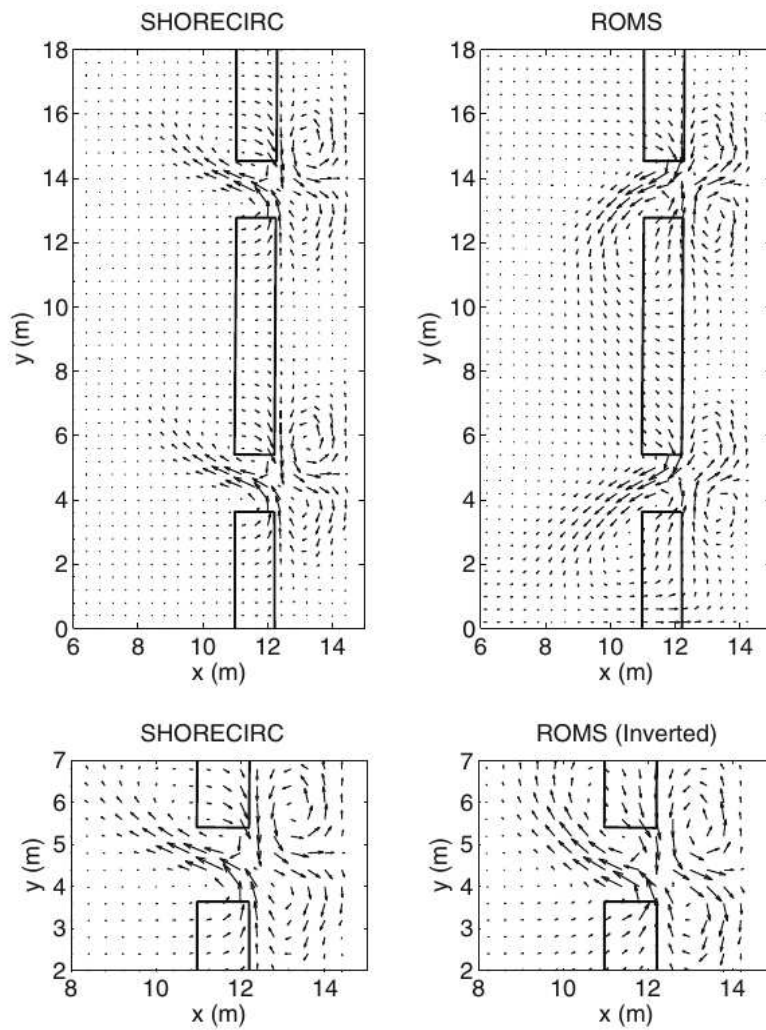
977
978 *Figure 14. Left: Mean wave height (cm) as a function of cross-shore distance. Right: Average surface*
979 *elevation (cm) depending on the cross-shore distance. In red: in the center of the basin ($y = 9$ m, with*
980 *bar). In blue: in the channel axis ($y = 13.6$ m).*

981
982 A second breaking zone is highlighted near the coast. This behaviour of the model is in good
983 agreement with the description of the process given in Haller et al. (2002). In the channel
984 axis, the wave height increases before the channel, as shown in Figures 13 and 14, because
985 of the blocking by the opposite rip current. Figure 15 shows the horizontal distribution of the
986 depth-averaged current, that is very similar to the circulation calculated with the phase-
987 averaged modelling presented by Haas et al 2003 (their figure 5) and Haas and Warner
988 2009 (their figure 7).

989

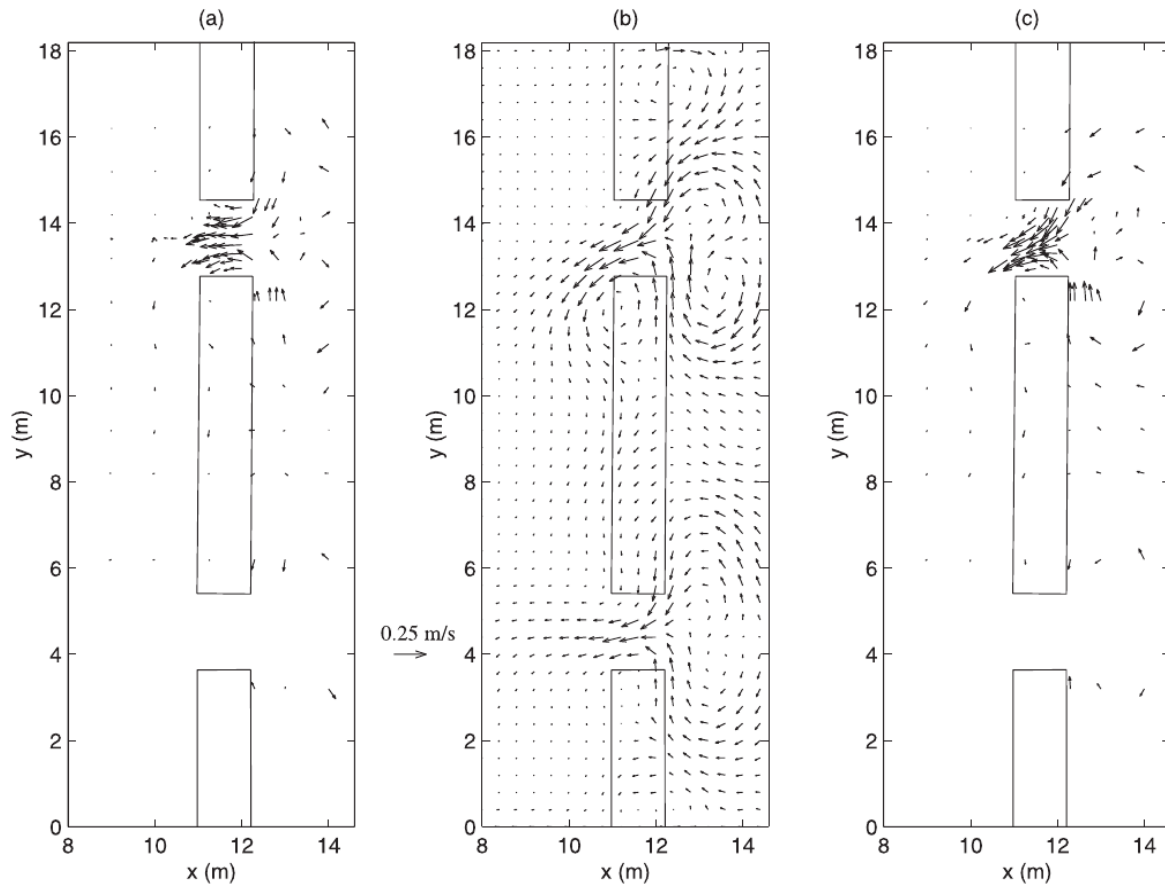


991 *Figure 15. Depth and time averaged current (m/s) computed by SYMPHONIE. Horizontal axis:*
992 *distance (m) cross-shore from the wave generator. Vertical axis: distance (m) alongshore.*



993

994 *Figure 15 continued: Figure 7 in Haas and Warner (2009). Depth-integrated mean currents.*



995

996 *Figure 15 continued: Figure 5 in Haas et al (2003). Time-averaged depth-integrated current from (a)*

997 *experimental data, (b) the simulation, and (c) the simulation at the same points as the experimental*

998 *data*

999

1000

1001 The rip current slows down the waves, causing the waves to refract toward the centre of the

1002 channel (Figure 13), in agreement with the visual observation of the laboratory experiment

1003 reported by Haas et al. (2003), hereafter H03, (see their section 6). However, the rip current

1004 does not lead to a wave breaking more important than the one above the bar. The wave

1005 height actually decreases more slowly in the channel than above the bar, so that in the last

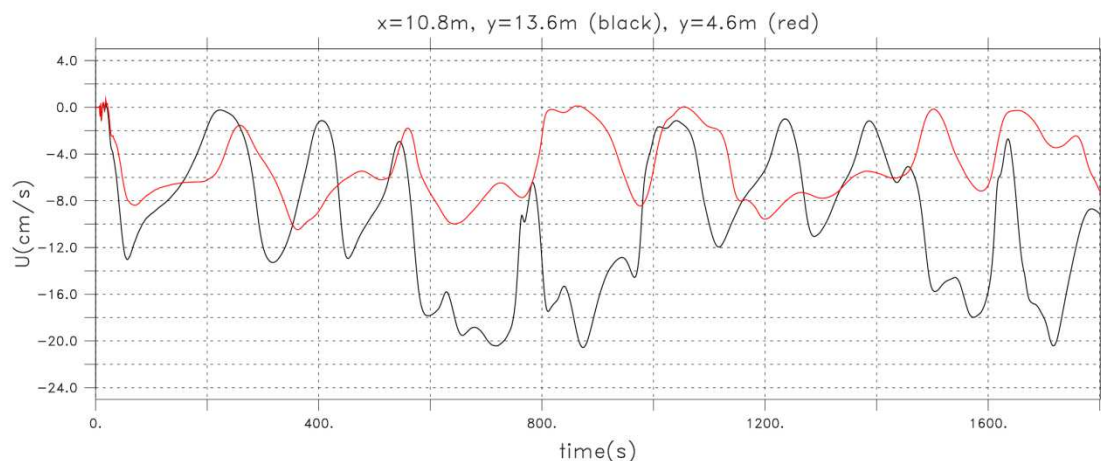
1006 meters before the coast the waves are higher in the channel axis than behind the bar (Figure

1007 14). The mean surface level increases at the coast, inducing a change in the average

1008 position of the water line allowed by the wetting-drying scheme of the model. The mean

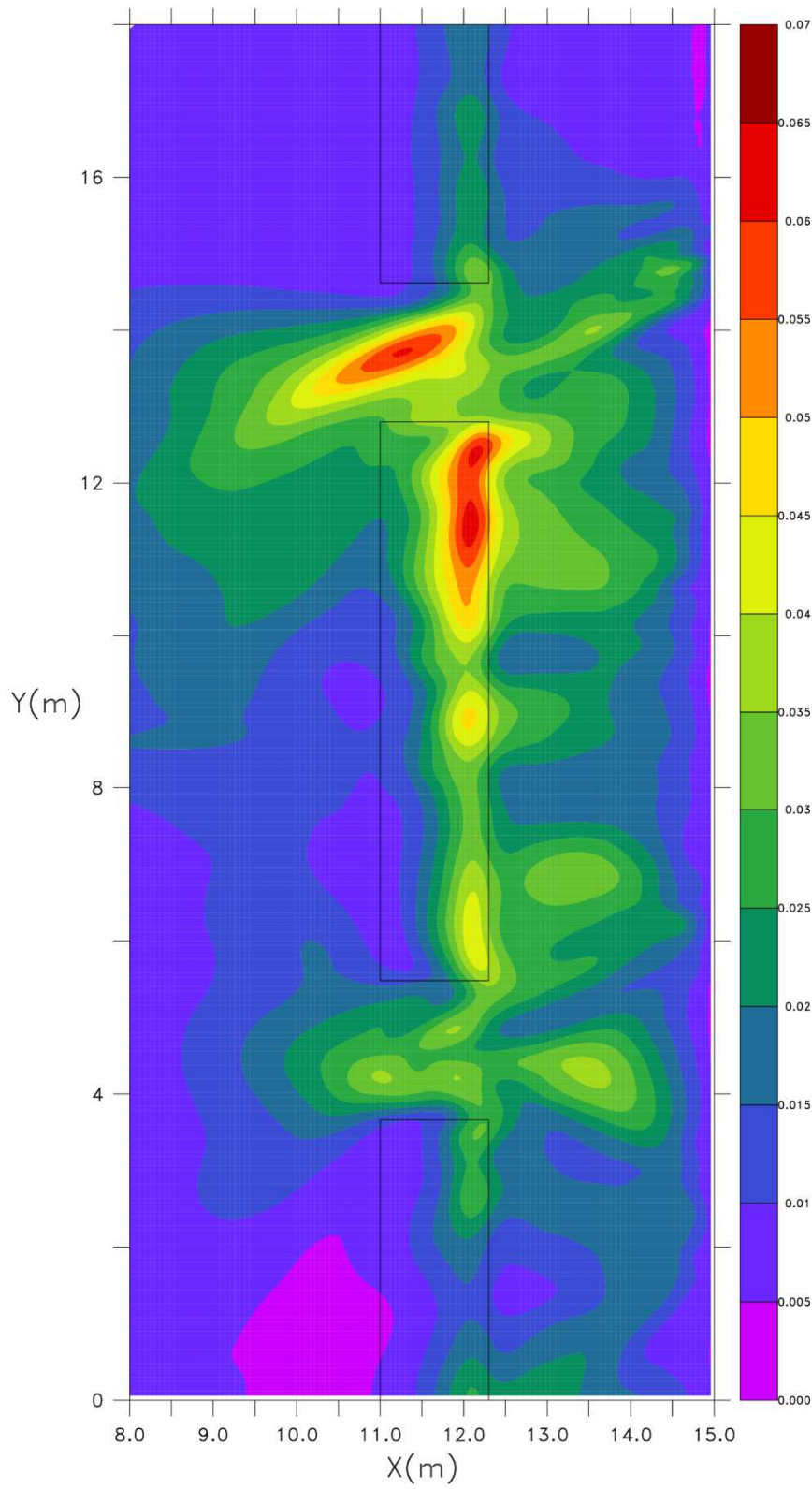
1009 surface level at the coast is markedly different in the channel axis and in front of the bar, in

1010 agreement with the observation (Figure 14). As Haas and Svendsen (2002) point out, this
 1011 difference is associated with a longshore pressure gradient that drives the flow to the
 1012 channels. Laboratory experiments show that rip currents are unstable and are characterized
 1013 by large temporal variations. The authors of these experiments emphasize the impossibility
 1014 of reproducing twice the same series of measurements, even if the experimental conditions
 1015 are a priori unchanged. An exact agreement with the model is therefore not sought.
 1016 Nevertheless, we expect from the model that it gives the correct orders of magnitude of the
 1017 rip currents and their variability. Figure 16 shows the temporal evolution of the current
 1018 averaged over the vertical and over a wave period in the two channels. Given the above
 1019 limitations, the agreement with the observations presented in H03 (see Figure 11.a in H03)
 1020 is good. The rip current at $y=4.6m$ is a little overestimated but, as in H03, it is mostly lower
 1021 than the rip current at $y=13.6m$. The latter has the good order of magnitude, with maximum
 1022 around 20 cm/s. The amplitude and time scale of its variability are also close to the
 1023 behaviour described in H03.



1024
 1025 *Figure 16. Cross-shore depth-averaged phase-averaged current (cm / s) in the two channels at*
 1026 *$x=10.8$ m as a function of time (s). Periods shorter than 1s are filtered. Negative values in the*
 1027 *direction of the wave generator. $y = 13.6m$ (black line), $y = 4.6m$ (red line).*
 1028

1029 The occurrence of the rip current is of the order of 200 seconds without being really regular.
1030 The variability of the rip current is of the order of a few centimetres per second, with a
1031 maximum standard deviation around 6cm/s in the centre of the channel at $y=13.5\text{m}$ and
1032 $x=11.5\text{m}$ (Fig.17).



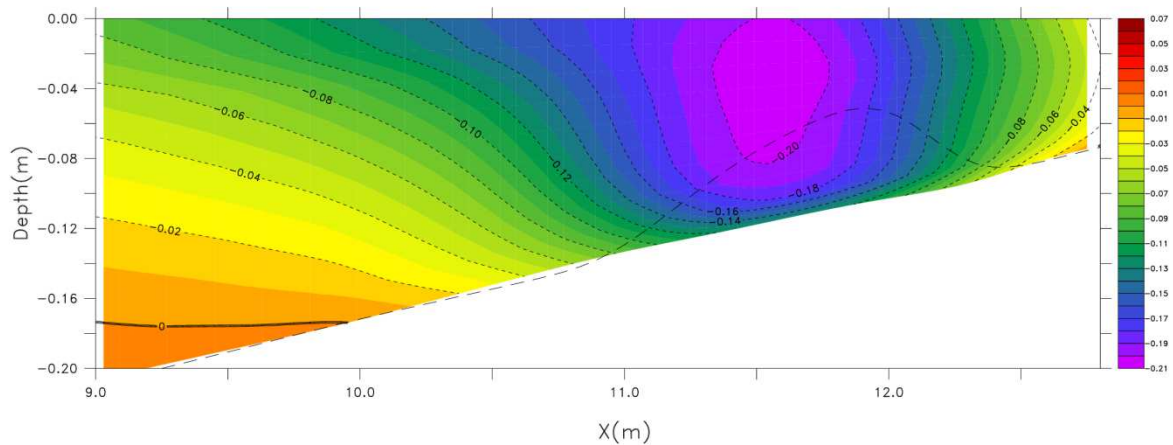
1033

1034 *Figure 17. Standard deviation of the cross-shore depth-averaged current (m/s)*

1035

1036
1037
1038
1039
1040
1041
1042
1043
1044
1045
1046

The vertical structure of the time-averaged cross-shore current in the rip channel (Fig.18) has similarities with the phase-averaged modelling of Haas and Warner (2009, their Figure 11) with a maximum intensity current around 0.2m/s between $x=11\text{m}$ and $x=12\text{m}$. At the point of maximum intensity ($x=11.5\text{m}$), the current is fairly homogeneous on the vertical except near the bottom where the current decreases strongly, in good agreement with the observation (Haas and Svendsen 2002, their figures 17, 18, 19). At the exit of the channel (offshore direction), the current decreases significantly. The vertical gradient also becomes larger and close to the bottom at $x=9\text{m}$ the current is even reversed (positive values in Fig.18), in good agreement with the observations (Haas and Svendsen 2002, their figures 13 and 14).



1047
1048
1049
1050
1051
1052
1053

Figure 18. time-averaged cross-shore current (m/s) at $y=13.6\text{m}$. Negative values are in the offshore direction (decreasing x).

5 Conclusions

1054 A phase-resolved wave model is derived from an ocean circulation model with the
1055 aim of performing simulations of current-wave interaction in nearshore areas. The model is
1056 evaluated on the fundamental aspects of wave dynamics, namely mainly the dispersion
1057 properties, the transformation of wave characteristics by bathymetry (shoaling, wave-
1058 breaking), the influence of waves on low frequency fields such as the mean surface levels
1059 and rip currents.

1060 With the exception of the post-breaking zone that can be processed in some models
1061 by a hydrostatic approach, the phase-resolved wave modelling requires a non-hydrostatic
1062 model. As the representation of the non-hydrostatic problem in all its complexity seems to be
1063 inevitably very expensive to date (Klingbeil et al, 2018), a scheme allowing a reasonable
1064 compromise between, on the one hand the extra cost of the computation, and on the other
1065 hand an acceptable loss of accuracy of non-hydrostatic properties of waves, has been
1066 introduced into the circulation model. It is shown that relative errors of less than a few % (on
1067 the dispersion relation and the vertical current profile) can be obtained with non-hydrostatic
1068 simulations costing 5 to 6 times more than a hydrostatic model calculated under the same
1069 conditions. The non-hydrostatic additional cost remains obviously high but low enough to
1070 consider simulations of realist events such as storms on very large areas and it is anyway
1071 worth noting that wave-current effect modelling based on a hydrostatic circulation model
1072 normally couple the latter with a phase-averaged wave model whose cost is possibly not
1073 negligible.

1074 The non-hydrostatic method implemented in the circulation model is derived from the
1075 method proposed by Lee et al. (2006). In practice, the classical Poisson problem is
1076 transformed into a pressure propagation equation. The resolution is iterative, local, and does
1077 not need to solve a system of linear equations. An essential aspect of this method is to
1078 properly control the various parameters related to the iterative aspect of the problem. The
1079 equation of pressure propagation depends on a constant (the latter being comparable to a
1080 propagation velocity) which determines the speed of the adjustment of the non-hydrostatic
1081 pressure to a change of the hydrostatic terms in the momentum equations. The precision of

1082 the non-hydrostatic behaviour depends on the fact that this adjustment is faster than the
1083 variation of the other fields. A meticulous adjustment of the time step of the model is in
1084 practice necessary, taking into account various parameters, including the wave propagation
1085 speed and a possible tuning [consisting in reducing the non-hydrostatic pressure gradient](#). So
1086 [far the reduction factor is a constant finding of a compromise in a set of possible values](#)
1087 [taking into account a range of periods and depths](#). Future development will adapt this tuning
1088 [to the wave peak period and bathymetry using the analytical reduction factor solution that](#)
1089 [this study established from the linearized ACM equations](#).

1090 The model is tested on idealized simulations and laboratory experiments. The ability
1091 of the non-hydrostatic method to accurately represent the dispersion properties of surface
1092 waves is first demonstrated in the context of the linear theory. Hamilton and Ebersole (2001)
1093 laboratory experiment is used to evaluate the model on the issue of wave height
1094 amplification associated with beach slope as well as wave breaking. The parameterization of
1095 the wave-breaking is based on momentum horizontal diffusion, trigger conditions being
1096 related to a Froude number. The tuning of the horizontal viscosity is consistent with
1097 considerations on the mechanical energy balance. The reasoning can be extended to the
1098 possible production of turbulent kinetic energy in the turbulent closure scheme, leading in
1099 practice to the increase in vertical turbulent viscosity. If the vertical profile of the residual
1100 alongshore current can apparently be slightly improved, on the other hand, the fraction of the
1101 kinetic energy lost by the breaking wave, which can in this way be injected into the vertical
1102 turbulence, remains uncertain for the authors and requires, obviously, to be better
1103 understood. [Along these lines, a part of the wave spectrum will still be missing in our future](#)
1104 [realistic applications because of the limited grid resolution \(the smallest periods being](#)
1105 [concerned\) with, as a result, a possible underestimation of the bottom stress in shallow](#)
1106 [areas that should be taken into account](#).

1107 Finally, the Haller et al. (2002) laboratory experiment, with its bar and its two
1108 channels, makes it possible to evaluate the model on the rip current problem. The model
1109 correctly reproduces rips currents and their high temporal variability. The feedback of the rip

1110 currents on the waves, in terms of wave amplification and refraction, is well represented. The
1111 onset of wave breaking is also well simulated, either above the bar or in the channel axis.

1112 This paper does not consider some 3D aspects as the effect of tracers on the
1113 pressure gradient and turbulence, which will be taken into account in future applications of
1114 this model. This also includes sediments that may be of great importance for modelling of rip
1115 currents as shown by Ma et al, 2014. These authors show that a wave-resolving non
1116 hydrostatic model is an efficient approach for the problem of resuspension of sediments by
1117 waves, and the possible feedback introduced by the modification of the equation of state by
1118 sediments, which can have a significant influence on the pressure gradient and the level of
1119 turbulence. [In practice our wave model will be coupled with the MUSTANG sediment model](#)
1120 [\(Le Hir et al, 2011\)](#)

1121 The next step is now to implement our model on realistic beaches, where we will
1122 confront the results with in situ data. Infragravity waves and the risk of submersion are
1123 possible applications. Some developments are still needed to provide a realistic wave
1124 spectrum to the boundary conditions of the phase-resolved wave model. The phase-
1125 averaged model, which can be applied over large domains at a reasonable cost, appears to
1126 be a good candidate for providing the boundary conditions to the phase-resolved model. [The](#)
1127 [phase-averaged wave model can also provide an estimate of the missing part of the wave](#)
1128 [spectrum in the deterministic model, helping the former to improve bottom turbulence in](#)
1129 [shallow areas](#). Finally, wave growth by local wind action will eventually be considered in the
1130 perspective of large areas (Deigaard and Nielsen, 2018).

1131

1132 **APPENDIX A**

1133

1134 The discrete version of $\frac{\partial^2 q}{\partial x^2}$ at the left-hand side of (4) is given by the left-side of:

1135

$$1136 \frac{q(x+dx)+q(x-dx)-2q(x)}{dx^2} = \frac{\partial^2 q}{\partial x^2} + \frac{dx^2}{12} \frac{\partial^4 q}{\partial x^4} + \dots \quad A1$$

1137

1138 The right-hand side of A1 is given by a Taylor development, $\frac{dx^2}{12} \frac{\partial^4 q}{\partial x^4}$ being the leading term of

1139 the errors made by the numerical scheme. Assuming a sinusoidal shape $(\frac{\partial^4 q}{\partial x^4} \approx k^4 q, k$ the

1140 wave number) leads to (5).

1141

1142

1143 **APPENDIX B: time stepping scheme**

1144

1145 The equations are calculated with a forward-backward time stepping scheme. The

1146 alternation of the fields along the time axis is presented in [Figure 19](#). The height of the

1147 surface at time t , η^t , is calculated first, knowing η^{t-1} and velocities at time $t-1/2$. Equation (9)

1148 gives q^t knowing q^{t-1} , q^{t-2} , and hydrostatic tendencies at time $t-1$. Note that the vertical

1149 laplacian of q is computed with an implicit centric scheme of the type $\frac{1}{2} \frac{\partial^2 q^{t-2}}{\partial z^2} + \frac{1}{2} \frac{\partial^2 q^t}{\partial z^2}$ so as not

1150 to limit the time step when the vertical mesh becomes very small (which becomes the case

1151 in sigma coordinates when the bathymetry tends to zero). The vertical velocity at time $t-1/2$,

1152 used for the advection terms of the equations for u and v , is computed from u and v at time $t-$

1153 $1/2$. Finally, the velocities at time $t + 1/2$ are calculated from the velocities, the sea surface

1154 height and the non hydrostatic pressure of the previous times. Vertical turbulent diffusion

1155 terms are calculated with an implicit scheme.

1156

$$q, \eta^{t-2} \quad u, v, w^{t-3/2} \quad q, \eta^{t-1} \quad u, v, w^{t-1/2} \quad q, \eta^t \quad u, v, w^{t+1/2}$$

1157

1158 *Figure 19: chronology of the variables of the model. At the beginning of each iterative cycle, the*

1159 *fields at time $t-1/2$ and time t are known.*

1160

1161

1162 **APPENDIX C**

1163

1164 The discrete version of the left-hand side of (30) is given by the left-side of:

1165

$$1166 \quad \frac{\eta(t+dt)+\eta(t-dt)-2\eta(t)}{dt^2} = \eta^{(2)}(t) + \frac{dt^2}{12}\eta^{(4)}(t) + \dots \quad C1$$

1167

1168 The right-hand side of C1 is given by a Taylor development, exponents in brackets indicating

1169 the order of the derivatives, $\frac{dt^2}{12}\eta^{(4)}(t)$ being the leading term of the errors made by the

1170 numerical scheme. Assuming a sinusoidal shape $\eta^{(4)}(t) \approx \omega^4\eta(t)$, ω the wave frequency)

1171 leads to $\frac{dt^2}{12}\eta^{(4)}(t) \approx \frac{dt^2}{12}\omega^4\eta(t)$. Similar reasoning can be done on the right-hand side of

1172 (30). The leading error term of the corresponding numerical scheme is , $c^2 \frac{dx^2}{12} \frac{\partial^4 \eta}{\partial x^4}$, equivalent

1173 (if a sinusoidal shape is assumed, k the wavenumber) to $c^2 \frac{dx^2}{12} k^4 \eta$ and $-c^2 \frac{dx^2}{12} k^2 \frac{\partial^2 \eta}{\partial x^2}$. Then

1174 reformulate (30) using the first two terms of the Taylor developments leads to (31).

1175

1176

1177 **APPENDIX D**

1178

1179 The potential energy flux is $F = gu\eta$ with $u = g\eta/c$. A sinusoidal form $\sin \Psi$ is assumed

1180 leading to $F = g^2 \frac{1}{c} \eta_0^2 \sin^2 \Psi$. A wave period averaging gives $F = g^2 \frac{1}{2c} \eta_0^2$. Within the wave

1181 breaking zone we assume $\frac{2\eta_0}{h} = \gamma$. Using $c = \sqrt{gh}$ leads to $F = \frac{1}{8} g^{3/2} \gamma^2 h^{3/2}$. The horizontal

1182 gradient is:

1183

$$1184 \quad \frac{\partial F}{\partial x} = \frac{3}{16} g^{3/2} \gamma^2 h^{1/2} \frac{\partial h}{\partial x} \quad D1$$

1185

1186 Consider a constant diffusion coefficient $\langle v_b \rangle$. The dissipation term due to horizontal
 1187 diffusion is $\varepsilon_b = -\langle v_b \rangle \left(\frac{\partial u}{\partial x} \right)^2$. Assuming a constant wavenumber leads to $\frac{\partial u}{\partial x} = k u_0 \cos \Psi$
 1188 and $\varepsilon_b = -\langle v_b \rangle k^2 u_0^2 \cos^2 \Psi$. A wave period averaging gives
 1189 $\varepsilon_b = -\langle v_b \rangle k^2 u_0^2 \frac{1}{2} = -\langle v_b \rangle k^2 \frac{1}{2} \left(\frac{g \eta_0}{c} \right)^2$. Using $\frac{2 \eta_0}{h} = \gamma$ leads to:

1190

$$1191 \quad \varepsilon_b = -\langle v_b \rangle \frac{1}{8} \left(\frac{k g \gamma h}{c} \right)^2 \quad \text{D2}$$

1192

1193 Using $k = \frac{\omega}{c} = 2\pi / (cT)$ (T the wave period), the equilibrium of (D1) and (D2) leads to (35)

1194

1195

1196

1197

1198

1199 **Acknowledgements**

1200

1201 The authors acknowledge the support of the SIROCCO team <http://sirocco.obs-mip.fr/>, the
 1202 NUMEROFIX project (NUmerical Modelling of Real Ocean surFace mIXing) funded by
 1203 LEFE/GMMC, the HPC resources from CALMIP (Grant 2018-P1325) and from GENCI and
 1204 CINES (Grand Equipement National de Calcul Intensif, project A0040110088).

1205

1206

1207 **References**

1208

1209 Arduin, F., Rasclé, N., Belibassakis, K., 2008. Explicit wave-averaged primitive equations
 1210 using a generalized Lagrangian mean, *Ocean Modelling*, 20, 35–60,
 1211 doi:10.1016/j.ocemod.2007.07.001.

1212
1213
1214
1215
1216
1217
1218
1219
1220
1221
1222
1223
1224
1225
1226
1227
1228
1229
1230
1231
1232
1233
1234
1235
1236
1237
1238
1239

Benetazzo A., Carniel S., Sclavo M., A. Bergamasco A., 2013. Wave–current interaction: Effect on the wave field in a semi-enclosed basin. *Ocean Modelling* 70, 152–165. <http://dx.doi.org/10.1016/j.ocemod.2012.12.009>

Bennis, A., Ardhuin, F., Dumas, F., 2011. On the coupling of wave and three-dimensional circulation models: Choice of theoretical framework, practical implementation and adiabatic tests, *Ocean Model.*, 40, 260–272.

Benoit, M., Raoult C., Yates M.L., 2017. .Analysis of the linear version of a highly dispersive potential water wave model using a spectral approach in the vertical. *Wave Motion* 74, 159–181.[doi:10.1016/j.wavemoti.2017.07.002](https://doi.org/10.1016/j.wavemoti.2017.07.002)

Berkhoff J., 1972. Computation of combined refraction-diffraction, in: Proc. 13th Int. Conf. on Coastal Eng., vol. 1, pp. 471–490.

Bertin, X., Bruneau, N., Breilh, J.-F., Fortunato, A. B., Karpytchev M., Importance of wave age and resonance in storm surges, The case Xynthia, Bay of Biscay, 2012. *Ocean Modelling*, Volume 42, Pages 16-30, ISSN 1463-5003, <https://doi.org/10.1016/j.ocemod.2011.11.001>.

Bertin, X., de Bakker, A., van Dongeren, A., Coco, G., André, G., Ardhuin, F., Bonneton, P., Bouchette, F., Castelle, B., Crawford, W. C., Davidson, M., Deen, M., Dodet, G., Guérin, T., Inch, K., Leckler, F., McCall, R., Muller, H., Olabarrieta, M., Roelvink, D., Ruessink, G., Sous, D. , Stutzmann, E., Tissier, M., 2018. Infragravity waves: From driving mechanisms to impacts. *Earth-Science Reviews* 177 (2018) 774–799. <https://doi.org/10.1016/j.earscirev.2018.01.002>

1240 [Blayo, E., Debreu, L., 2005. Revisiting open boundary conditions from the point of view of](#)
1241 [characteristic variables. Ocean Modelling 9, 231–252.](#)
1242

1243 Blumberg, A.F., Mellor, G.L., 1987. A description of a three-dimensional coastal circulation
1244 model. In: Heaps, N. (Ed.), Three-Dimensional Coastal Ocean Models, Coastal Estuarine
1245 Science, vol. 4. American Geophysical Union, pp. 1–16.
1246

1247 Bonneton, P., Chazel, F., Lannes, D., Marche, F., Tissier, M., 2011a. J. Comput. Phys., 230,
1248 1479-1498, DOI:10.1016/j.jcp.2010.11.015
1249

1250 Bonneton, P., Barthelemy, E., Chazel, F., Cienfuegos, R., Lannes, D., Marche, F., Tissier,
1251 M., 2011b. Recent advances in Serre–Green Naghdi modelling for wave transformation,
1252 breaking and runup processes, 2011b. European Journal of Mechanics - B/Fluids, 30, 589-
1253 597, <https://doi.org/10.1016/j.euromechflu.2011.02.005>.
1254

1255 Bouharguane A., Azerad P., Bouchette F., Marche F., Mohammadi B., 2010. Low complexity
1256 shape optimization & a posteriori high fidelity validation. Discrete & Continuous Dynamical
1257 Systems - B, 13 (4) : 759-772. doi: [10.3934/dcdsb.2010.13.759](https://doi.org/10.3934/dcdsb.2010.13.759)
1258

1259 Bordois, L., Auclair, F., Paci, A., Dossmann, Y., and Nguyen, C., 2017. Nonlinear processes
1260 generated by supercritical tidal flow in shallow straits. Physics of Fluids,
1261 <http://dx.doi.org/10.1063/1.4986260>
1262

1263 Bruneau, N., 2009. Modélisation morphodynamique des plages sableuses, Ph.D. thesis,
1264 Université Bordeaux I.
1265

1266 Castelle, B., Scott, T., Brander, R.W., McCarroll R.J., 2016. Rip current types, circulation
1267 and hazard, In Earth-Science Reviews, Volume 163, Pages 1-21, ISSN 0012-8252,
1268 <https://doi.org/10.1016/j.earscirev.2016.09.008>.
1269

1270 Costa, A., Doglioli, A. M., Marsaleix, P., Petrenko A. A., 2017. Comparison of in situ
1271 microstructure measurements to different turbulence closure schemes in a 3-D numerical
1272 ocean circulation model. Ocean Modelling. <https://doi.org/10.1016/j.ocemod.2017.10.002>
1273

1274 Deigaard, R. and Nielsen, P., 2018. Wind generation of waves: Energy and momentum
1275 transfer - An overview with physical discussion, Coastal Engineering, 139, 36-46,
1276 <https://doi.org/10.1016/j.coastaleng.2018.04.024>.
1277

1278 Feddersen, F., Trowbridge, J.H., 2005. The Effect of Wave Breaking on Surf-Zone
1279 Turbulence and Alongshore Currents: A Modelling Study. Journal of physical oceanography.
1280 2187- 2203
1281

1282 Feddersen, F., Trowbridge, J.H., Williams III, A.J., 2007. Vertical Structure of Dissipation in
1283 the Nearshore. Journal of Physical Oceanography. 37, 1764-1777.
1284 <http://dx.doi.org/10.1175/JPO3098.1>
1285

1286 Guérin, T., Bertin, X., Coulombier, T., de Bakker, A., 2018. Impacts of wave-induced
1287 circulation in the surf zone on wave setup, Ocean Modelling, 123, 86-97,
1288 <https://doi.org/10.1016/j.ocemod.2018.01.006>.
1289

1290 Green, A.E., Naghdi, P.M., 1976. A derivation of equations for wave propagation in water of
1291 variable depth. J. Fluid Mech., 78, 237-246
1292

1293 Haller, M. C., Dalrymple, R. A., Svendsen, I. A., 2002. Experimental study of nearshore
1294 dynamics on a barred beach with rip channels, *J. Geophys. Res.*, 107(C6), doi:
1295 10.1029/2001JC000955.

1296

1297 Hamilton, D. G., and B. A. Ebersole, 2001. Establishing uniform longshore currents in a
1298 large-scale sediment transport facility, *Coastal Engineering*, 42 , 199–218.

1299

1300 Haas, K. A., and I. A. Svendsen, 2002. Laboratory measurements of the vertical structure of
1301 rip currents, *J. Geophys. Res.*, 107(C5), doi: 10.1029/2001JC000911.

1302

1303 Haas, K. A., Svendsen, I. A., Haller, M. C. Zhao, Q. 2003. Quasi-three-dimensional
1304 modelling of rip current systems, *J. Geophys. Res.*, 108, 3217, doi: 10.1029/2002JC001355,
1305 C7.

1306

1307 Haas, K. A., Warner, J. C., 2009. Comparing a quasi-3D to a full 3D nearshore circulation
1308 model: SHORECIRC and ROMS, *Ocean Modelling*, Volume 26, Issues 1–2, 91-103,
1309 <https://doi.org/10.1016/j.ocemod.2008.09.003>.

1310

1311 Kanarska, Y., Maderich, V., 2003. A non-hydrostatic numerical model for calculating free-
1312 surface stratified flows. *Ocean Dyn.* 53 (3), 176–185.

1313

1314 Kanarska, Y., Shchepetkin, A., McWilliams, J. C., 2007. Algorithm for non-hydrostatic
1315 dynamics in the Regional Oceanic Modelling System, In *Ocean Modelling*, Volume 18,
1316 Issues 3–4, 143-174, <https://doi.org/10.1016/j.ocemod.2007.04.001>.

1317

1318 Kennedy, A. B., Chen, Q., Kirby, J. T., Dalrymple, R. A. 2000. Boussinesq modelling of wave
1319 transformation, breaking and runup. I: 1D. *J. Waterw., Port, Coastal, Ocean Eng.*, 1261, 39–
1320 47.

1321

1322 [Kinsman, B., 1965. Wind waves: Their Generation and Propagation on the Ocean Sur-](#)
1323 [face. Courier Dover Publications.](#)

1324

1325 Kirby, J.T. and Dalrymple, R.A., 1983. A parabolic equation for the combined refraction-
1326 diffraction of Stokes waves by mildly-varying topography, *Journal of Fluid Mechanics*, 136,
1327 453-466.

1328

1329 Kirby, J.T., Wei, G., Chen, Q., Kennedy, A., Dalrymple, R.A., 1998. FUNWAVE 1.0; Fully
1330 Nonlinear Boussinesq Wave Model Documentation and User's Manual. Newark, Delaware:
1331 Center for Applied CoastResearch, University of Delaware, Research Report CACR-98-06.

1332

1333 Klingbeil, K., Burchard, H., 2013. Implementation of a direct nonhydrostatic pressure
1334 gradient discretisation into a layered ocean model, *Ocean Modelling*, 65, 64-77,
1335 <https://doi.org/10.1016/j.ocemod.2013.02.002>

1336

1337 Klingbeil, K., Debreu, L., Lemarié, F., Burchard, H., 2018. The numerics of hydrostatic
1338 structured-grid coastal ocean models: state of the art and future perspectives. *Ocean*
1339 *Modelling*.

1340

1341 Kumar, N., Feddersen, F., Uchiyama, Y., McWilliams, J., O'Reilly, W, 2015. Midshelf to
1342 Surfzone Coupled ROMS–SWAN Model Data Comparison of Waves, Currents, and
1343 Temperature: Diagnosis of Subtidal Forcings and Response. *J. Phys. Oceanogr.*, Vol. 45,
1344 pp. 1464-1490, DOI: 10.1175/JPO-D-14-0151.1

1345

1346 Lee, J.W., Teubner, M.D., Nixon, J.B., Gill, P.M., 2006. Application of the artificial
1347 compressibility method for turbulent open channel flows. *International Journal for Numerical*
1348 *Methods in Fluids* 51, 617–633.

1349

1350 [Le Hir P., Cayocca F., Waeles B., 2011. Dynamics of sand and mud mixtures: A](#)
1351 [multiprocess-based modelling strategy. Continental Shelf Research, 31, 135-149.](#)

1352 <https://doi.org/10.1016/j.csr.2010.12.009>

1353

1354 Lemarié, F., Debreu, L., Madec, G., Demange, J., Molines, J.M., Honnorat, M., 2015.
1355 Stability constraints for oceanic numerical models: implications for the formulation of time
1356 and space discretizations, *Ocean Modelling*, 92, 124-148,
1357 <https://doi.org/10.1016/j.ocemod.2015.06.006>.

1358

1359 Lynett, P., 2006: Nearshore wave modelling with high-order Boussinesq-type equations. *J*
1360 *Waterw Port C-ASCE*, 132, 348–357, doi:10.1061/(ASCE)0733-950X(2006)132:5(348).

1361

1362 Mahadevan, A., Olinger, J., Street, R., 1996. A nonhydrostatic mesoscale ocean model parts
1363 1, 2, *J. Phys. Oceanogr.* 26 (9), 1868–1900.

1364

1365 Marshall, J., Hill, C., Perelman, L., Adcroft, A., 1997. Hydrostatic, quasi-hydrostatic, and
1366 nonhydrostatic ocean modelling. *J. Geophys. Res.* 102, 5733–5752.

1367

1368 Ma, G., Shi, F., Kirby, J. T., 2012. Shock-capturing non-hydrostatic model for fully dispersive
1369 surface wave processes. *Ocean Modelling*, 43–44, 22-35,
1370 <https://doi.org/10.1016/j.ocemod.2011.12.002>.

1371

1372 Ma, G., Chou, Y.-J., Shi, F., 2014. A wave-resolving model for nearshore suspended
1373 sediment transport. *Ocean Modelling*, 77, 33-49,
1374 <https://doi.org/10.1016/j.ocemod.2014.03.003>.

1375

1376 Magne, R., Ardhuin, F., Rey, V., Herbers, T. H. C., 2005. Topographical Scattering of
1377 Waves: Spectral Approach. *Journal of Waterway, Port, Coastal & Ocean Engineering*. Vol.
1378 131 Issue 6, p311-320. 10p. 15 Charts. DOI: 10.1061/(ASCE)0733-950X(2005)131:6(311)
1379

1380 [Marsaleix P., Auclair F., Estournel C., 2006, Considerations on Open Boundary Conditions](#)
1381 [for Regional and Coastal Ocean Models. *Journal of Atmospheric and Oceanic Technology*,](#)
1382 [23,1604-1613, <http://dx.doi.org/10.1175/JTECH1930.1>](#)
1383

1384 Marsaleix, P., Auclair, F., Floor, J. W., Herrmann, M. J., Estournel, C., Pairaud, I., Ulses, C.,
1385 2008. Energy conservation issues in sigma-coordinate free-surface ocean models. *Ocean*
1386 *Modelling*. 20, 61-89. <http://dx.doi.org/10.1016/j.ocemod.2007.07.005>
1387

1388 Marsaleix, P., Auclair, F., Duhaut, T., Estournel, C., Nguyen, C., Ulses, C., 2012.
1389 Alternatives to the Robert-Asselin filter. *Ocean Modelling*, 41, 53-66
1390 <http://dx.doi.org/10.1016/j.ocemod.2011.11.002>
1391

1392 McKiver, W. J., Sannino, G., Braga, F., Bellafiore, D., 2016. Investigation of model capability
1393 in capturing vertical hydrodynamic coastal processes: a case study in the north Adriatic Sea.
1394 *Ocean Science*, 12, 51–69, <http://dx.doi.org/10.5194/os-12-51-2016>
1395

1396 McWilliams, J. C., Restrepo, J. M., Lane, E. M., 2004. An asymptotic theory for the
1397 interaction of waves and currents in coastal waters, *J. Fluid Mech.*, 511, 135 – 178.
1398

1399 Mellor, G., 2003. The Three-Dimensional Current and Surface Wave Equations. *Journal of*
1400 *Physical Oceanography*, Vol. 33 Issue 9, p1978. 12p.
1401

1402 Michaud, H., Marsaleix, P., Leredde, Y., Estournel, C., Bourrin, F., Lyard, F., Mayet, C.,
1403 Ardhuin, F., 2012. Three-dimensional modelling of wave-induced current from the surf zone
1404 to the inner shelf. *Ocean Science*, 8, 657-681. <http://dx.doi.org/10.5194/os-8-657-2012>
1405

1406 Miche, A., 1944: Mouvements ondulatoires de la mer en profondeur croissante ou
1407 décroissante. forme limite de la houle lors de son déferlement. application aux digues
1408 maritimes. Troisième partie. Forme et propriétés des houles limites lors du déferlement.
1409 Croissance des vitesses vers la rive. *Annales des Ponts et Chaussées*, Tome 114, 369-406.
1410

1411 Oger, G., 2006. Aspects théoriques de la méthode SPH et applications à l'hydrodynamique
1412 à surface libre, PhD Thesis, Ecole Centrale de Nantes, France.
1413

1414 Paluszkiwicz, T., Garwood, R.W., Denbo, D.W., 1994. Deep convective plumes in the
1415 ocean. *Oceanography* 7(2):37–44, <http://dx.doi.org/10.5670/oceanog.1994.01>.
1416

1417 Petrenko A., Dufau C., Estournel C., 2008, Barotropic eastward currents in the western Gulf
1418 of Lion, north-western Mediterranean Sea, during stratified conditions. *Journal of Marine*
1419 *Systems*, 74, 406-428, doi:10.1016/j.jmarsys.2008.03.004
1420

1421 Raoult, C., Benoit, M., Yates, M. L., 2016. Validation of a fully nonlinear and dispersive wave
1422 model with laboratory non-breaking experiments. *Coastal Engineering*, 114, 194–207
1423 doi:10.1016/j.coastaleng.2016.04.003.
1424

1425 Rodi, W., 1987. Examples of calculation methods for flow and mixing in stratified fluid. *J.*
1426 *Geophys. Res.*, 92, 5305–5328.
1427

1428 Roeber, V. and Cheung, K. F., 2012. Boussinesq-type model for energetic breaking waves in
1429 fringing reef environments. *Coastal Engineering*, 70:1–20.

1430

1431 Rouillet, G., Molemaker, M. J., Ducouso, N., Dubos, T., 2017. Compact symmetric Poisson
1432 equation discretization for non-hydrostatic sigma coordinates ocean model, *Ocean*
1433 *Modelling*, 118, 107-117, <https://doi.org/10.1016/j.ocemod.2017.09.001>.

1434

1435 Rusu, E., Soares, C. G., 2013. Modelling Waves in Open Coastal Areas and Harbors with
1436 Phase-Resolving and Phase-Averaged Models. *Journal of Coastal Research*, Vol. 29, No. 6.
1437 DOI: 10.21121/JCOASTRES-D-11-00209.1

1438

1439 Serre, F., 1953. Contribution à l'étude des écoulements permanents et variables dans les
1440 canaux. *La Houille Blanche*, 3 (6), 374-388

1441

1442 Shi, J., Shi, F., Kirby, J. T., Ma, G., Wu, G., Tong, C., Zheng J., 2015. Pressure Decimation
1443 and Interpolation (PDI) method for a baroclinic non-hydrostatic model, In *Ocean Modelling*,
1444 Volume 96, Part 2, Pages 265-279, ISSN 1463-5003,
1445 <https://doi.org/10.1016/j.ocemod.2015.09.010>.

1446

1447 Soulsby, R., 1995. Bed shear stresses due to combined waves and currents. In: Stive, M.,
1448 Fredsøe, J., Hamm, L., Soulsby, R., Teisson, C., Winterwerp, J. (Eds.), *Advances in Coastal*
1449 *Morphodynamics*. Delft Hydraulics, Delft, The Netherlands, pp. 420–423.

1450

1451 Svendsen, I. A., Qin, W., Ebersole, B. A., 2003. Modelling waves and currents at the LSTF
1452 and other laboratory facilities. *Coastal Engineering* 50, 19 – 45.
1453 [http://dx.doi.org/10.1016/S0378-3839\(03\)00077-2](http://dx.doi.org/10.1016/S0378-3839(03)00077-2)

1454

1455 Tissier, M., Bonneton, P., Marche, F., Chaze, I F., Lannes, D., 2012. A new approach to
1456 handle wave breaking in fully non-linear Boussinesq models, *Coastal Engineering*, 67, 54-
1457 66, <https://doi.org/10.1016/j.coastaleng.2012.04.004>.

1458

1459 Tolman, H. et al. 2016. User manual and system documentation of WAVEWATCH III (R)
1460 version 5.16.NOAA/NWS/NCEP/MMAB Tech. Note. 329. 326 pp. +Appendices

1461

1462 Uchiyama, Y., McWilliams, J. C., Restrepo, J. M., 2009, Wave–current interaction in
1463 nearshore shear instability analyzed with a vortex force formalism, *J. Geophys. Res.*, 114,
1464 C06021, doi:10.1029/2008JC005135.

1465

1466 Uchiyama, Y., McWilliams, J. C., Shchepetkin, A. F., 2010. Wave–current interaction in an
1467 oceanic circulation model with a vortex-force formalism: Application to the surf zone, *Ocean*
1468 *Model.*, 34, 16–35, doi:10.1016/j.ocemod.2010.04.002.

1469

1470 Uchiyama, Y., J. C. McWilliams, Akan, C., 2017. Three-dimensional transient rip currents:
1471 Bathymetric excitation of low-frequency intrinsic variability, *J. Geophys. Res. Oceans*, 122,
1472 5826–5849, doi:10.1002/2017JC013005.

1473

1474 Weir, B., Uchiyama, Y., Lane, E. M., Restrepo, J. M., Williams, J. M., 2011. A vortex force
1475 analysis of the interaction of rip currents and surface gravity waves, *J. Geophys. Res.*, 116,
1476 C05001, doi:10.1029/2010JC006232.

1477

1478 Yoon, J. J., 2014. Non-hydrostatic Modelling of Waves Transformation and Rip Current
1479 circulation: A case Study for Haeundae Beach, Korea. *Journal of Coastal Research*, 72, 184-
1480 189.

1481

1482 Zijlema, M., Stelling, G., Smit, P., 2011. SWASH: An operational public domain code for
1483 simulating wave fields and rapidly varied flows in coastal waters. *Coastal Engineering*, 58,
1484 992-1012, <https://doi.org/10.1016/j.coastaleng.2011.05.015>.

1485

1486 Zhou, Z., Hsu, T.-J., Cox, D., Liu, X., 2017. Large-eddy simulation of wave-breaking
1487 induced turbulent coherent structures and suspended sediment transport on a barred beach.
1488 Journal of Geophysical Research: Oceans 122 (1), 207-235. doi: [10.1002/2016JC011884](https://doi.org/10.1002/2016JC011884)